Sustained neurotrophic factor cotreatment enhances donor and host retinal ganglion cell survival in mice

Jonathan R. Soucy,[1,2,#] Emil Kriukov,[1,2,#] Julia Oswald,[1,2] Monichan Phay,[1,2] John Masland,[1,2] Christian Pernstich,[3] Petr Baranov[1,2,*]

1. Massachusetts Eye and Ear, Boston, MA
2. Department of Ophthalmology, Harvard Medical School, Boston, MA
3. Cell Guidance Systems, Cambridge, UK

[#]Co-first authors

*Corresponding author: petr_baranov@meei.harvard.edu

Abstract:

Retinal ganglion cells (RGCs) lack regenerative capacity in mammals, and their degeneration in glaucoma leads to irreversible blindness. The transplantation of stem cell-derived RGCs lacks clinically relevant effect due to insufficient survival and integration of donor cells. We hypothesize that the retinal microenvironment plays a critical role in this process, and we can engineer a more acceptable setting for transplantation. Since the adult mammalian retina does not have regenerative capacity, we turned to the developing human retina to reconstruct cell-cell interactions at a single-cell level. We established a human fetal retina atlas by integrating currently available single-cell RNA sequencing datasets of human fetal retinas into a unified resource. We align RGC transcriptomes in pseudotime to map RGC developmental fate trajectories against the broader timeline of

retinal development. Through this analysis, we identified brain-derived neurotrophic factor (BDNF) and glial-derived neurotrophic factor (GDNF) as key factors in RGC survival, highly expressed during fetal development but significantly reduced in adulthood despite the persistence of their receptors. To demonstrate the practical application of these findings, we show that using a slow-release formulation of BDNF and GDNF enhances RGC differentiation, survival, and function in vitro and improves RGC transplantation outcomes in a mouse model. BNDF/GDNF co-treatment not only increased survival and coverage of donor RGCs within the retina but also showed neuroprotective effects on host RGCs, preserving retinal function in a model of optic neuropathy. Altogether, our findings suggest that manipulating the retinal microenvironment with slow-release neurotrophic factors holds promise in regenerative medicine for treating glaucoma and other optic neuropathies. This approach not only improves donor cell survival and integration but also provides a neuroprotective benefit to host cells, indicating a significant advancement for glaucoma therapies.

Introduction:

The loss or degeneration of retinal ganglion cells (RGCs) in glaucoma is a leading cause of irreversible blindness worldwide, with no current therapies available to restore vision once these cells are lost *(1)*. While RGCs, the neurons in the retina that relay all visual information from the eye to the brain, can regenerate in some lower vertebrates, they have no capacity for regeneration in the mammalian retina *(2)*. Cell transplantation has been proposed as a potential solution to replace RGCs lost in advanced retinal disease,

but poor cell survival rates post-transplantation have limited the effectiveness and further development of this strategy *(3–6)*.

The glaucomatous retina is typically characterized by increased intraocular pressure (IOP), which can cause inflammation, immune cell infiltration, and host cell reactivity *(7, 8)*. Even after the IOP normalizes, the altered microenvironment with hyperactive glia can persist *(8)*, making it challenging for transplanted donor cells to survive in the host retina. Further, after transplantation, donor cells encounter an environment that lacks adequate oxygenation and metabolic support until they structurally integrate into their respective positions within the host retina. This deficiency can intensify the stress experienced by the donor cells, leading to further decreased survival rates. To overcome these limitations and establish a more favorable microenvironment, we investigate the developing human fetal retina through single-cell transcriptomics to identify pro-survival factors present during retinogenesis and then deliver those factors into the retina to improve donor RGC survival after transplantation.

Specifically, we established a human fetal retinal atlas by integrating currently available human fetal retina single-cell RNA sequencing datasets *(9, 10)* into a single resource to provide a detailed understanding of the retina and RGCs during development. However, because RGCs express unique developmental transcriptomes within the same canonical time points to represent RGC development rather than retinal development, we aligned RGC transcriptomes in pseudotime. By analyzing both pseudotime for RGC-specific development and canonical time for retinal development, we identified brain-derived neurotrophic factor (BDNF) and glial-derived neurotrophic factor (GDNF) as being highly expressed during development but no longer present during adulthood despite the

continued expression of their receptors. Through our in silico analysis, we further demonstrate that BDNF and GDNF are necessary to prevent apoptosis and host RGCs are the primary source of endogenous BDNF in the retina, suggesting that supplementing transplants with exogenous neurotrophic factors may improve donor RGC survival in an RGC-depleted retina.

After identifying BDNF and GDNF as essential regulators of RGC survival during development, we show that slow-release BDNF and GDNF can improve the RGC differentiation yield and survival in retinal organoids in vitro. Furthermore, we demonstrate that slow-release BDNF and GDNF improve the structural and functional characteristics of human stem cell-derived RGCs in vitro. We then confirm that co-delivery of mouse and human stem cell-derived RGCs with slow-release formulations of BDNF and GDNF improves donor RGC coverage within the retina and the total number of cells that survive post-transplantation. Lastly, we demonstrate that a slow-release formulation of BDNF and GDNF provides a neuroprotective effect on host RGC, preventing a decrease in electroretinogram-related response caused by glutamate-induced neurotoxicity.

Methods:

Single-cell RNA Sequencing Data Processing

Single-cell RNA sequencing data analysis was performed in RStudio v. 2023.06.1 Build 524 (R language v. 4.3.1) using previously published datasets from the human fetal retina (from Week 8 to Week 27) *(9)*. The raw Cell ranger output data was processed independently following the standard Seurat pipeline with a few differences: for

FindNeighbors() and RunUMAP(), dims = 50. For multiple stages, the analysis included both the peripheral and central retina. Individual Seurat objects are stored separately in the data availability folder.

Data Integration and Atlas Generation

To integrate the datasets upon independent processing of every object, we follow the integration pipeline from Seurat v.4, which includes the steps of SelectIntegrationFeatures(), FindIntegrationAnchors(), IntegrateData(), and a custom script for the dataset processing in the same manner as for the independent datasets from the previous step.

To annotate the cell types, we manually annotated the data by identifying variable features for every Seurat cluster. This was later confirmed by integrating our data with the human brain cortex atlas from the Azimuth HubMAP source to prove the neuronal identity using the prediction score. The annotated cell types gave us insights into the type frequency information obtained by merging the time points within every 4-week step. The frequency was calculated as several cells per cell type to the total number of cells in the dataset of the relevant time point. For further data analysis, the Azimuth approach and the AzimuthReference() and SCTransform() functions can be used to use this atlas as a reference tool and build a representative UMAP embedding with automated cell type annotation.

Cell-cell interactions analysis

To obtain the information related to incoming and outgoing cluster ligand-receptors interactions, we used the CellChat package (v. 2.1.0) for every time point using our atlas as previously described *(11, 12)*. To avoid the projection reducing the dropout effects of signaling genes, particularly for possible zero expression of subunits of ligands/receptors, we used raw.use = FALSE setting in computeCommunProb function. Total heatmaps for the incoming and outgoing signaling and chord diagrams for the signaling of interest were generated. Additionally, we used LRLoop, following the default pipeline, to calculate the communication levels of every ligand-receptor pair in the package database per time point to build the patterns of communication across development. We labeled the retinal ganglion cells cluster as a cluster of interest while the rest of the populations were merged into one group.

<u>Python Data Transformation and ForceAtlas2-scFates pseudotime application</u>

Once the atlas was generated, we converted it from.h5Seurat to .h5ad format for the Python-dependent downstream analysis (Python v. 3.7). We used scanpy to generate ForceAtlas2-based embedding for the RGC subset of the atlas with n_eigs = 3 and additional palantir-based preprocessing. With the embedding to be generated, we reconstructed the cell fate trajectory using the scFates package *(13)*. On that trajectory, pseudotime values were quantified, and RGCs were split into t_factor groups with the pseudotime values order. With the in-built scFates functions, we found variable genes on the cell fate trajectory of RGC development. The metadata, including pseudotime and t_factor clustering, was exported to be added to the Seurat object with the AddMetaData() function in Seurat.

Downstream Analysis

The atlas with additional metadata was used for the further GSEA pathway analysis in Python. We selected multiple pathways from the Molecular Signatures Database related to retinal ganglion cell function and performed the enrichment to visualize it with the canonical time points and t_factor (pseudotime groups) as metadata. For the GOBP_NEURAL_RETINA_DEVELOPMENT, GOBP_APOPTOTIC_PROCESS_INVOLVED_IN_DEVELOPMENT, GOBP_AXON_ DEVELOPMENT, GOBP_AXON_EXTENSION, GOBP_NEURON_ MATURATION, and GOBP_NEURON_MIGRATION pathways, we obtained the gene list to build dot plots and ridge enrichment plots split by both canonical time points and t_factor clusters.

Furthermore, we established a list of neurotrophic ligands and their potential receptors from currently available ligand-receptor databases. We generated heatmaps and expression dynamics plots to show the trend of neurotrophic receptor expression across development (for both canonical time points and pseudotime).

To show the changes in gene expression for different time points, the AverageExpression function in Seurat was applied to the whole dataset. Trends for GFRA1 and NTRK2, neurotrophic receptors, as well as GDNF and BDNF, their ligands, average expression at different time points plots were visualized using ggplot2 (v. 3.3.6) and ggalt (v. 0.4.0) packages *(14)*.

The analysis also included a step with a correlation between the expression of NTRK2, BDNF receptor, GFRA1, GDNF receptor, and apoptosis pathway genes. To obtain the

gene list for apoptosis, we downloaded the annotation from the Molecular Signatures Database (http://www.gsea-msigdb.org/gsea/msigdb/human/geneset/HALLMARK_APOPTOSIS.html).

To check the apoptosis pathway expression, we used the escape package (v. 1.6.0) *(15)*. We merged subsetted RGCs populations in FD59, FD82, and FD125 Seurat objects and performed the enrichment on the RNA count data using the enrichIt function with the ssGSEA method *(16)*. To examine the correlation between NTRK2/GFRA1 and the apoptosis pathway expression, we generated a plot using FeatureScatter Seurat function for the GFRA1 positive and NTRK2 positive cells. We added a regression model to the analysis using the geom_smooth function with the 'lm' method.

<u>Mouse Stem Cell-derived RGC Differentiation</u>

Mouse stem cell-derived RGCs were differentiated using a 3D retinal organoid approach as previously described *(5, 17)*. Induced pluripotent stem cells (iPSCs) derived from Tg[Thy1.2-Green Fluorescent Protein (GFP)]M mice were cultured on gelatin-coated (0.2% v/v) flasks in standard culture conditions (37°C, >95% humidity, 5% CO2). Mouse stem cell maintenance (mSCM) medium [10% fetal bovine serum (FBS), 1x L-glutamine, 1x non-essential amino acids, 1x sodium pyruvate, 1x antibiotic-antimycotic, 1x EmbryoMax Nucleosides, 100 μM β-Mercaptoethanol, and 100 U/mL mouse leukemia inhibitory factor in DMEM/F12 (3500 mg/L dextrose)] was replaced every two days until the iPSC colonies approached approximately 70% confluency. Upon reaching 70% confluency, iPSCs were harvested using 1x trypsin-EDTA and either transferred to new gelatin-coated flasks at a density of 2000 cells/cm² or used for retinal ganglion cell (RGC)

differentiation as previously detailed. For RGC differentiation, 1500 cells were initially seeded in 50 µL of Optic Vesicle (OV) medium [1x L-glutamine, 1x non-essential amino acids, 1x sodium pyruvate, 1x antibiotic-antimycotic, 1x lipid concentrate, 0.2x Insulin-Transferrin-Selenium-Ethanolamine, 100 µM β-Mercaptoethanol, 1.5% FBS, 1 µM N-Acetyl-L-cysteine (NAC), and 10 µM forskolin in DMEM/F12 (3500 mg/L dextrose)] per well in uncoated 96-well U-bottom polystyrene plates. After 24 hours in standard culture conditions, each well received an additional 50 µL of OV medium with 2% Matrigel to start forebrain/retinal differentiation. The next day, 100 µL of OV medium with 1% Matrigel was added to each well. The organoids were maintained in this medium until the ninth day of differentiation, with half of the medium being replaced every two days. On day 9, the organoids were extracted from the plates, randomly sectioned to isolate optic vesicles for expanded growth, and transferred to low-attachment flasks. From this point, they were kept in Optic Cup (OC) medium [1x L-glutamine, 1x non-essential amino acids, 1x sodium pyruvate, 1x antibiotic-antimycotic, 1x lipid concentrate, 100 µM β-Mercaptoethanol, 1x B27 without vitamin A, 1 µM N-Acetyl-L-cysteine (NAC), and 10 µM forskolin in DMEM/F12 (3500 mg/L dextrose)]. Half the medium was replaced every other day until days 21 to 24 of retinal maturation. Starting from day 16, the OC medium was supplemented with 250nM all-trans-retinoic acid.

<u>Human Stem Cell-derived RGC Differentiation</u>

Colonies of H9-BRN3B:tdTomatoThy1.2-hESCs were cultured on six-well plates coated with 2% Matrigel with mTeSR1 media in a low oxygen incubator (5% CO_2, 3.5% O_2, above 95% humidity, 37°C). Media was replaced daily. When the cell density reached

around 70% after 4-5 days, the cells were detached using accutase for 8 minutes at room temperature and transferred to a new Matrigel-coated plate at a ratio between 1:10 and 1:20.

Human RGCs were differentiated in 3D retinal organoid cultures as previously described *(17–19)*. During cell passaging, hESC colonies were enzymatically dissociated for 12 minutes to form a single-cell suspension. To create embryoid bodies, 7,500 hESCs per well were seeded in an ultra-low attachment 96-well U-bottom plate in a low oxygen incubator for 24 hours. After 24 hours, the plate was moved to standard culture conditions. The differentiation media was exchanged daily and transitioned from a 3:1 mix of mTeSR1 and BE6.2-NIM [B27 + E6 at 2X concentration – neural induction medium: 1x L-glutamine, 1x sodium pyruvate, 1x antibiotic-antimycotic, 1x B27 without Vitamin A, 0.88 mg/mL NaCl, 38.8 mg/L insulin, 128 mg/L L-ascorbic acid, 28 µg/L selenium, 21.4 mg/L transferrin, and 38.8 mg/L $NaHCO_3$ in DMEM/F12 (3500 mg/L dextrose)] to primarily BE6.2-NIM by day 8. To support neural and early retinal development, the media was supplemented with 20 µM Y-27632 on day 0, 1% Matrigel from days 2 to 6, 3µM IWR-1-endo from days 1 to 4, and 55 ng/mL BMP4 on day 6. On day 8, organoids were randomly sectioned to isolate optic vesicles, facilitating growth and keeping size under the diffusion limit (1.4 mm diameter). These chopped organoids were then placed on tissue culture-treated plastic in Long-Term Retinal Differentiation Media (LT-RDM) [1x L-glutamine, 1x sodium pyruvate, 1x antibiotic-antimycotic, 1x B27, 1x non-essential amino acids, and 10% FBS in 50:50 1x DMEM/F12 (3500 mg/L Dextrose):DMEM (4500 mg/mL dextrose)] to encourage attachment and retinal epithelium growth. The media was replaced every two days, transitioning to a 1:1 mix of LT-RDM and Retinal Differentiation Media (RDM)

[LT-RDM without FBS] by day 17, with added 100nM smoothened agonist (SAG) from days 12 to 16. On day 17, the retinal tissue clusters were detached and moved to a poly(2-hydroxyethyl methacrylate)-coated flask for suspension culture in RDM supplemented with 100nM SAG. From day 18 onwards, the media, now a 1:3 mix of LT-RDM and RDM with 2.5% FBS and 100nM SAG, was replaced every other day, gradually transitioning to pure LT-RDM by day 24. From day 26, the media was supplemented with 1mM taurine, and from day 32, 250nM all-trans-retinoic acid. The LT-RDM was replaced every other day until retinal organoids were collected for dissociation.

RGC Isolation

To dissociate mature mouse (d21 – 24) and human retinal organoids (d44 – 48), the embryoid body dissociation kit from Miltenyi Biotec (catalog number 130-096-348) was used with the gentleMACS™ Dissociator, following the instructions provided by the manufacturer, with a single adjustment. The preset gentleMACS programs EB_01 and EB_02 were substituted with Brain_01 and Brain_02, respectively. After dissociation, mouse and human RGCs (Thy1.2-positive cells) were isolated by magnetic microbead-based sorting using the Dynabeads™ FlowComp™ Mouse Pan T (CD90.2) Kit from Invitrogen (catalog number 11465D), following the manufacturer's instructions.

Flow Cytometry

Dissociated cells were resuspended in 4% paraformaldehyde and fixed for 30 minutes on ice. Post-fixation, cells were centrifuged at 300 x g for 5 minutes and resuspended in

isolation buffer [2 mM EDTA, 2% FBS, and 0.1% bovine serum albumin in Hank's Balanced Salt Solution without Ca2+ and Mg2+] for flow cytometric analysis. The samples were analyzed using a MACSQuant Analyzer 10 flow cytometer. The data were gated based on forward/side scatter and cell area/height using FlowJo software. This approach was designed to exclude small particulate debris and multi-cell aggregates from the analysis.

Donor RGC Transplantation

Donor RGC transplantations were performed at the Schepens Eye Research Institute. All animal work was approved by the Institutional Animal Care and Use Committee (IACUC) *(17)*. To support donor RGCs and establish a proneuronal microenvironment, we formulated our mouse or human donor RGCs with selected pro-survival factors. To avoid repeated intraocular injections, which could cause additional inflammation and reduce donor RGC viability, we formulated donor RGCs with slow-release BDNF and GDNF using the Polyhedrin Delivery System (PODS® Human BDNF and PODS® Human GDNF (Cell Guidance Systems, PPH1-50 and PPH2-50). Donor RGCs were transplanted (10,000 – 20,000 RGCs/retina) into adult (1- to 4-month-old) RGC-deficient mouse retinas (inherited loss or neurotoxic model) with and without BDNF- and GDNF-loaded PODS under a general (ketamine/xylazine intraperitoneal injections) and local (0.5% proparacaine eye drops) anesthetic. Donor RGC suspensions (1 μL) were injected intravitreally using a beveled glass microneedle with an inner diameter of 80 μm at a flow rate of 1 μL per minute. Mice were kept on a standard 12-hour light-dark cycle and were euthanized at predetermined endpoints—2 weeks for transplants from the same species

(syngeneic) and 3 days for cross-species (xenotransplantation) transplants—using CO2 inhalation. Three to fourteen days after transplantation, eyes were enucleated, fixed for 24 hours at room temperature in 4% paraformaldehyde, and then processed for retinal flat-mount preparation. Retinas were stained for host and donor cells to assess RGC survival and neurites (8 – 11 mice/group). Specifically, eyes were enucleated after three days for human donor RGC transplants to minimize immune reactions typical of xenotransplantation and after fourteen days for mouse donor RGCs to allow for neurite outgrowth.

Electroretinogram

To measure functional recovery following transplantation, mice were injected with NMDA 1 week prior to intravitreal injection of donor RGCs to cause RGC death and subsequently received either cells alone, cells+PODS, or PODS alone. Electroretinography (ERG) was performed six weeks post-transplant to assess host retinal function. Before recording electrical activity in the retina with ERG, mice were dark-adapted overnight. Mice were then anesthetized with ketamine (120 mg/kg) and xylazine (20 mg/kg), administered intraperitoneally with a 25G needle. The pupils of each mouse were dilated using 1% Tropicamide, followed by the application of Genteal to maintain corneal moisture. Mice were positioned on a temperature-controlled platform on the ERG machine (Diagnosys LLC). Reference and ground electrodes were placed under the skin on the forehead and tail, respectively. Two gold-ring electrodes were carefully positioned on the corneas without blocking the pupil. A drop of artificial tear solution was applied to ensure hydration throughout the experiment. The positive scotopic threshold response (pSTR) data were

gathered using a series of flashes, averaging 40 responses for each intensity level. The pSTR was quantified by measuring the amplitude from the baseline to the peak of the positive wave. Post-ERG, the eyes were treated with antibiotic ointment and artificial tears. The mice were then placed on a warming pad with a circulation of heated water to stabilize their body temperature, allowing for a safe recovery.

Immunohistochemistry

To visualize RGCs in culture, retinal flat-mounts, and retinal sections, samples were fixed for 30 min for cell culture and >4 hours for tissue samples with 4% (v/v) paraformaldehyde at room temperature. For retinal sections, eyes were sent to the Schepens Eye Research Institute Morphology Core for paraffin embedding (producing 6 μm thick sections) and Hematoxylin and Eosin (H&E) staining. The paraffin-embedded sections were first treated with an xylene substitute, followed by ethanol washes. Antigen retrieval was then performed using a sodium citrate buffer (10 mM Sodium citrate, 0.05% Tween-20, pH 6.0) for 30 minutes.

For immunofluorescence staining, samples were incubated overnight (>12 hours) at 4°C with 1:400 goat anti-mouse secondary antibody in blocking buffer (10% goat serum, 1% bovine serum albumin, 0.1% sodium citrate, 0.25% Tween-20, 0.25% Triton-X, and 0.3M glycine in 1x phosphate-buffered saline) to reduce non-specific staining. Following blocking, the RGCs and retinal tissues were incubated with primary antibodies in staining buffer (1% bovine serum albumin, 0.25% Tween-20, and 0.25% Triton-X in 1x PBS) for 48 to 72 hours at 4°C. A complete list of primary antibodies and their concentrations is provided in Table S2. Post-primary antibody incubation, tissues were washed three times

in wash buffer (0.1% Tween-20, 0.1% Triton-X in 1x PBS) to remove unbound antibodies. Secondary antibodies (goat anti-chicken, goat anti-rabbit, and goat anti-mouse) were added at a 1:500 dilution in staining buffer and incubated for 12 to 24 hours at 4°C. Following another triple wash, the samples were stained with 1 µg/mL DAPI in PBS for 20 minutes to highlight cell nuclei. To reduce tissue autofluorescence, samples were treated with 10 mM copper sulfate (pH 5.0) at room temperature for 15 minutes. After a final PBS rinse, the samples were mounted between glass cover slides and coverslips using a polyvinyl alcohol-based mounting medium containing an antifade agent (1,4-Diazabicyclo[2.2.2]octane). Imaging was performed using an Olympus IX83-FV3000 confocal microscope.

Enzyme-linked immunosorbent assay (ELISA)

BDNF ELISA (Boster #EK0307) was performed according to the manufacturer's protocol. PBS solution (50 µl) containing either 1e6, 5e5, 2e5, 5e4, or 1e4 PODS® BDNF was added to wells of a 96-well plate and was spun down at 3000 g for 25 min. PBS was removed, and the plate was dried in a laminar flow cabinet. RPMI 1640 Complete Medium supplemented with 10% bovine calf serum was added to each well (100 µl/well). The plate was then incubated at 37 °C, 5% CO2. For the release time curve, medium from wells with 1e6 PODS® was collected on days 1, 2, 3, 4, and 7 after medium addition and stored at -20 °C. For the dose-response curve, the medium was collected on day 4 after medium addition.

Extracellular recordings

Human stem cell-derived RGC neural activity was quantified using a high-density multielectrode array (HD-MEA). HD-MEA chips (MaxOne, MaxWell Biosystems) consist of 26,400 electrodes arranged in a 120 × 220 configuration with 17.5 µm center-to-center electrode spacing to create a 3.85 × 2.10 mm2 sensor area *(20)*. Each HD-MEA chip was cleaned using a 1%-Terg-a-zyme-solution, sterilized with 70% ethanol, and coated with 0.1 mg/mL Poly-D-Lysine (PDL) in 1x borate buffer and 0.025 mg/mL laminin in N2B27 [1x GlutaMAX, 1x antibiotic antimycotic, 1% N2 supplement, and 2% B27 supplement in 50:50 1x DMEM/F12:Neurobasal media] before use. RGCs (~5 uL, 20,000 RGCs/uL) were seeded directly onto the sensor area of each MEA chip at a density of ~12,500 RGCs/mm2 with or without BDNF- and GDNF-loaded PODS (150 PODS/µL) and allowed to attach in standard culture conditions for 2 hours. After attachment, 1 – 2 mL N2B27 was added to each chip (depending on the chip dimensions), and 50% of the media was replaced every other day.

After 18 – 20 days in culture, cell culture media was replaced with warmed BrainPhys™ media 1 hour before extracellular recording. Spontaneous neural activity was recorded from donor RGCs using the MaxOne HD-MEA system (MaxWell Biosystems). The MaxOne HD-MEA system was placed in a cell culture incubator (37°C, >95% humidity, 5% CO2) during the recordings, and RGC activity was recorded using the MaxLab Live software (MaxWell Biosystems).

For all recordings, first, an Activity Scan Assay was performed in 'checkered scan mode' using a 5 – 5.5σ spike threshold to identify the active electrodes. Activity scans in 'checkered scan mode' provide an optimal balance between speed and resolution to

identify possible neural units (RGCs with spontaneous activity). After generating an activity map, a Network Assay was performed to simultaneously record from ~120 neural units for 5 minutes. Each neural unit consists of a 9 x 9 electrode configuration centered on active electrodes with the highest firing rate.

Spike sorting was performed on the 5-minute Network Assay recordings using the SpikeInterface framework and the SpykingCircus2 algorithm to identify individual neurons from each neural unit *(21, 22)*. Recordings were preprocessed using a Bandpass filter with a minimum and maximum frequency of 300 and 3000 Hz and a common mean referencing technique. Spike sorting was performed using the default parameters, except the radius was increased to 250 μm. The spike sorting output was automatically curated, and neurons were removed if they had a presence ratio less than 90% or an amplitude medium below 20 μV. RGC firing rate and spike amplitude were reported as the mean of a minimum of five MEA chips for the Control and PODS groups.

Statistical Analysis

Statistical significance was calculated using GraphPad PRISM 10 using an unpaired t-test or a Tukey one-way ANOVA. Error bars represent the mean ± SD of measurements (*$P < 0.05$, **$P < 0.01$, ***$P < 0.001$, and ****$P < 0.0001$). Each dot within a bar plot represents an individual retina/mouse or well/MEA.

Data Availability Statement

The software and packages used for the analysis can be found in Table S1. The code used for this study to reproduce the bioinformatical analysis is available on GitHub at https://github.com/mcrewcow/fetal_retina_PODS_Soucy_Kriukov. The GitHub repository provides detailed instructions on every step of the analysis and the code to reproduce the computational analysis. To obtain the data generated in this study, please refer to the relevant repository folder or contact the corresponding authors. This data may include individual Seurat objects, integrated atlas, reference atlas (SCT) version, Python cell fate reconstructed RGC subset, individual and integrated CellChat objects, and the gene/ligand-receptor lists generated throughout the analysis.

To make our discoveries more transparent and available, we deposited the atlas for the public audience on the CellxGene platform. This allows users to perform basic data analysis in the web browser. The atlas (current v. 1) is available by the following link: https://cellxgene.cziscience.com/collections/c11009b8-b113-4a99-9890-78b2f9df9d79

Please contact the corresponding author for the Seurat and CellChat files in '.rds' format.

Results:

Establishing a Human Fetal Retinal Atlas to Study Cellular Communication Dynamics in Development

By engineering the adult retinal microenvironment to resemble key developmentally relevant molecular features, we aim to improve donor RGC survival. While RGCs are the

first-born neurons in the retina, the role of other cells in the retina, including progenitors, and the retinal microenvironment itself in RGC development remains unknown. To understand this phenomena, we sourced, reanalyzed, and integrated published human fetal and adult retina single-cell RNA sequencing data to establish a human fetal retinal atlas *(9, 10)*. We demonstrate the atlas of developing retina (108,838 cells) from fetal week 8 to 27 with one-week sample resolution. We performed cluster identification using published single-cell RNA sequencing data to define each retinal population throughout development based on their cell type-specific genes (**Figure 1A-B**). As a resource to the community, we also described the complete dynamics of regulons (**Figure S1-2**), transcriptional motifs, and cell-cell interactions (**Figure S3**) in the resolution available using LRLoop, CellChat *(11, 12)*, and pySCENIC *(23)*. Within the resolution, we cover every cell class information on the currently available ligand-receptor database in CellChat v. 2 *(12)* and regulons and motifs from the cisTarget 2017 motif collection database for hg19.

Separating these data according to their canonical timepoint (**Figure 1B**), we show different cellular compositions during each stage of retinal development, with RGCs comprising the largest percentage of retinal neurons from weeks 8 to 11 (**Figure 1C-D**). As the retina further develops, the percentage of retinal progenitors and precursor cells is reduced while the other populations of retinal neurons increase (**Figure 1D**). Together, these data based on single-cell RNA sequencing match those quantifying the cells arising at different developmental stages *(24)*. However, unlike the histological and cell sorting approaches used to understand neuron birth order in the retina, by establishing a human

fetal retinal atlas, we can explore cellular communication to and from each individual cell population, as well as their gene profiles and the tissue as whole *(11)*.

To validate that we are capturing all the cellular communication in the retina during development, we show increased interactions throughout development (**Figure 1E**). By exploring individual ligand-receptor pairing at each canonical timepoint, we can see these interactions are broadly classified into four groups: starts high, remains high; starts high, goes lower; starts low, goes higher; and starts low, remains low (**Figure 1F**). We can hypothesize which interactions are important to best support a specific cell type by matching these patterns to the prevalence of that cell (**Figure 1D**). For example, because the prevalence of RGCs is greatest during early development, we predict that receptor-ligand pairs classified into the starts high and goes lower group is necessary for RGC development. Lastly, we can also delve deeper into a single to study the involvement of individual cell populations (**Figure 1G**), highlighting the importance of those cell-cell interactions during development. A complete panel of all those cell-cell interactions is available in **Figure S3**.

Pseudotime Analysis Reveals Developmental Heterogeneity and Key Neurotrophic Receptor Expression in Retinal Ganglion Cells

While all cells are the same canonical age during development, they are not necessarily the same developmentally. To better understand the RGC-specific communication that drives this development within the retina, we performed a pseudo-time analysis on the ForceAtlas2 embedding using the scFates package cell fate trajectory reconstruction pipeline *(13)*. As expected, this approach allows us to disentangle the maturation state

heterogeneity at each canonical time point by ordering the cells from the least to the most mature (**Figure 2A, Figure S4**). These RGCs were shown to express variable genes along the pseudotime trajectory by their maturation state (**Figure S5**). We then separated the continuous pseudotime timeline into the sectors from t_1 to t_7 for further analysis following the Leiden clustering algorithm *(25)* (**Figure 2B**).

To confirm that pseudotime ordering allows better maturation resolution, we compare the canonical and pseudotime expression profiles for select genes from the neural retina development pathway (GOBP_NEURAL_RETINA_DEVELOPMENT). We demonstrate that select genes, such as ATOH7, GAP43, and POU4F2, show a random or stable expression pattern if grouped by canonical timepoint but a gradient in their expression if split by pseudotime sectors (**Figure 2C**). Using Gene Set Enrichment Analysis, we visualized the complete neural retina development pathway, containing 80 genes, and demonstrated the same switch for non-paternal to gradient expression during development (**Figure 2D**). Similar gradient expression patterns can also be observed in several tissue- and cell-level RGC pathways during development (**Figure S6**).

While studying gene expression according to its canonical time point is essential for understanding the tissue microenvironment, quantifying gene expression in pseudotime is necessary when studying individual cells due to the heterogeneity of cell maturation states. Therefore, we built a heatmap of all known neurotropic receptors with pseudotime resolution to understand which receptors RGCs express at different stages of development (**Figure 2E**). As expected, we observe receptor expression patterns in pseudotime that we cannot confirm with the heterogeneity present in the canonical time points. For instance, receptors like FZD3 and IGF1R are mostly related to early retinal

differentiation *(26, 27)*, but this is only apparent in pseudotime with their highest expression in the t_1-t_3 state (**Figure 2E**).

With our goal of engineering the retinal microenvironment with ligands to support RGC survival, we wanted first to understand which receptors are expressed on mature RGCs. From our neurotrophic receptor heatmap, we could only identify fewer than ten receptors using canonical time but more than 25 receptors using pseudotime. Of those, only GFRA1 had continuous expression in mid-late retina development (t_2-t_7), while NTRK2 had a specific late expression pattern (t_6-t_7). Further highlighting the importance of using pseudotime to understand expression in mature RGCs, GFRA1 and NTRK2 expression in canonical time showed the highest expression in week 14 and week 16, respectively, but no expression at week 27 (**Figure 2F**).

BDNF and GDNF are Key Neurotrophic Factors in Retinal Development and RGC Survival

To determine which molecular features were present within the retina during development but not during adulthood, we performed an in silico analysis of the single-cell transcriptome of developing human retinas within the spectrum of developmental stages (FD59, FD82, FD125). Specifically, we evaluated changes in gene expression of every previously identified neurotropic factor over time and identified Brain-Derived Neurotrophic Factor (BDNF) and Glial Cell-Derived Neurotrophic Factor (GDNF) as genes of interest that fit this profile and whose receptors are highly expressed in mature RGCs (**Figure 2F**). Both these factors were prominently expressed during the early stages of retinal development, particularly in phases where RGCs undergo differentiation

and maturation (**Figure 3A**). However, their levels markedly diminish as the retina matures, indicating we may need to supplement the retina with these proneuronal factors to reestablish an environment to support RGC repopulation.

Furthermore, by examining the relationship between BDNF/GDNF expression and apoptosis pathway (HALLMARK_APOPTOSIS) genes, we found a clear negative correlation (**Figure 3B**), indicating that higher levels of BDNF and GDNF are associated with reduced activation of cell death pathways. This relationship underscores the potential of these neurotrophic factors in promoting RGC survival, especially in conditions where these cells are at risk, such as in glaucoma.

We then analyzed ligand-receptor interactions to understand the communication pathways involving BDNF and GDNF using CellChat *(11, 12)*. This analysis provided insights into how these factors signal within the retinal environment, distinguishing between autocrine signaling, where cells respond to the signals they emit, and paracrine signaling, involving communication between different cell types. Since our analysis shows that RGCs are the primary source of BDNF and GDNF in the retina (**Figure 3C**), their loss in diseases like glaucoma creates an environment that is further lacking these crucial survival factors. Supplementing transplanted cells with BDNF and GDNF could not only enhance the survival of these cells but also potentially rejuvenate the surrounding retinal tissue, creating a more favorable environment for transplantation, regeneration, and repair.

Modifying the Retinal Microenvironment with Slow-release BDNF and GDNF Improves RGC Transplantation Outcomes and Preserves Host RGC Function after an Induced Optic Neuropathy

To avoid rapid clearance of BDNF and GDNF in our transplant setting, we utilize a slow-release formation of BDNF and GDNF (BDNF and GDNF-loaded polyhedrin-based particles (PODS)). BDNF and GDNF-loaded PODS show approximately 50 pg/mL sustained growth factor release in culture over a week (**Figure S7**). To mimic RGC loss in glaucoma, we utilized two RGC loss models for transplantation, NMDA-induced toxicity and an inherited loss model (**Figure S8**). Our transplantation experiments in these mice demonstrated that delivering BDNF/GDNF-PODS with stem cell-derived mouse RGCs significantly improved the transplantation outcome. The success rate of mouse donor RGC transplantations, defined as a transplant with more than 0.5% of delivered donor RGCs surviving *(5)*, increased to 73% from 37% with the co-treatment of BDNF/GDNF-PODS. Moreover, the PODS formulation led to a 2.7-fold increase in donor mouse RGC coverage across the retina (**Figure 4A-B**). Several neurites extend toward and into the optic nerve head (**Figure 4C-D**). This finding is critical as it demonstrates that the transplanted cells have the potential to connect with their postsynaptic targets in the brain, a necessary step for functional recovery after injury.

To measure retinal function after transplantation, we measure the positive scotopic threshold response using electroretinography (ERG) to evaluate RGCs *(28, 29)*. While our mouse stem cell-derived RGCs were shown to be functional by Ca2+ imaging (**Figure S9**), these ERG results indicate that Thy1-GFP+ donor RGCs alone don't rescue retinal function at six weeks post-transplantation in the NMDA model of toxic optic neuropathy

(**Figure 4E**). However, treatment with PODS and cells+PODS led to the partial preservation of RGC function as measured by pSTR response at six weeks (32uV in the PODS group vs. 17uV in the control group, **Figure 4E**), indicating that PODS may provide a neuroprotective effect on host RGCs.

In addition to mouse stem cell-derived RGC transplantation, to improve the clinical relevance of this work, we transplanted human stem cell-derived RGCs with and without PODS. To limit the immune responses caused by xenotransplantation, mouse retinas were explanted 3 days post-transplantation. Although the PODS co-treatment did not affect the success rate of human donor RGC transplantation, the PODS formulation led to a 15-fold increase in the total number of human donor RGCs detected in the mouse retina (**Figure 5A-C**). Despite only 3 days of growth post-transplantation, 50% of all transplants containing PODS showed donor RGC neurites extending toward the optic nerve head, with an average length of 1008.44 ± 264.12 μm compared to 10% in the control group (**Figure 5D-E**). Critically, these results demonstrate the potential of PODS to improve the survival and integration of transplanted human RGCs, which could lead to functional recovery in patients with retinal degeneration. Donor RGC axon outgrowth and morphology, including entry into the optic nerve head, was enhanced by PODS co-treatment, proposing a benefit of co-treatment for cell delivery.

BDNF and GDNF Treatment Improves RGC Structural and Function Maturation *In Vitro*

Growth factors have been widely described for aiding in the survival and differentiation of neurons in vitro *(30)*. Therefore, we also investigated the role of these neurotropic factors

in RGC differentiation. Including BDNF and GDNF PODS in our mouse RGC differentiation resulted in a greater than 50% increase in Thy1.2+ve cells population within late-stage (D27) organoids compared to non-treated controls (**Figure S10**).

Moreover, RGCs exhibit complex neurite morphology within the adult human retina. Qualitatively, PODS co-treatment led to an apparent increase in neurite morphological complexity post-transplantation (**Figure 4C and 5A-B**). To demonstrate that PODS co-treatment directly affected neurite length, we culture our human stem cell-derived RGCs in vitro and show a significant increase in neurite length with PODS co-treatment (**Figure 6A-B**).

Lastly, we examined the ability of human stem cell-derived RGCs to fire spontaneous action potentials, which is an analogy for functional maturation *(31)*. To detect spontaneous action potentials, we measure RGC electrophysiology using a high-density multielectrode array (MEA). Human stem cell-derived RGCs were seeded on an MEA with and without PODS and cultured for three weeks. Due to the high-density nature of the MEA, individual RGC actional potentials were recorded from multiple electrodes simultaneously (**Figure 6C**). To resolve individual neurons, we performed spike sorting before analyzing the data (**Figure S11**). We detected no spontaneous action potentials within the first week of culture; however, by 18 – 20 days, human donor RGC exhibited a robust firing response. Those RGCs cultured with PODS significantly increased their median spike amplitude and mean firing rate compared to controls. PODS co-treatment resulted in a 45.5 μV median spike amplitude and 0.90 Hz mean firing rate compared to 36.1 μV and 0.44 Hz in the control (**Figure 6D-E**).

Discussion:

Blindness and vision impairments resulting from the loss or degeneration of retinal ganglion cells (RGCs) are irreversible. While the underlying pathology of optic neuropathies is diverse (e.g., elevation of intraocular pressure, acute trauma), all phenotypically resemble neurodegenerative disease *(32)*. Initially, patients experience a decrease in the visual field, dyschromatopsia, and changes in pupillary response, gradually progressing toward complete vision loss *(33)*. Optical coherence tomography and other live imaging approaches have demonstrated that RGC death in glaucoma is slow *(34)*. Therefore, the timely application of pro-survival factors may preserve the remaining function and potentially reverse some vision loss *(35–37)*.

These factors and pathways can be discovered through high-throughput phenotypic screening, loss-of-function animal models, or studying actively remodeling developing/regenerating systems *(38–40)*. Alternatively, our human fetal retina atlas offers a valuable resource for discovering novel factors and targets that affect cellular processes, such as cell migration, maturation, and synapse formation. Searching for these targets may start by studying the dynamics of cell class development and understanding the cell fate drivers of timepoint-specific factors. The current version of the atlas offers a broad spectrum of high-throughput data in the aspects of cell-cell interactions, regulons, and transcriptional motifs for every cell class at every time point. With that, many potential applications exist that increase the borders of factors search from intrinsic gene expression changes to ligand-receptor pairs, communication patterns between cell classes, variable regulons, and further motifs analysis in connection with other available methods, such as ChIP-, ATAC-seq, GWAS, and Hi-C. Since this atlas

demonstrates the first evidence of regulons and motifs (list available upon request) in human developing retina, it could give clues for population-related studies.

Beyond subtype-specific heterogeneity, cells are also developmentally heterogeneous. This developmental heterogeneity adds complexity to identifying relevant factors, making pseudotime analysis more appropriate than canonical time points. RGCs exhibit heterogeneity in states at any given moment, with gene dynamics observable through pseudotime methods. Grouping by pseudotime rather than time points reveals state-related targets applicable to ligand-receptor pairs, regulons, and motifs analyses. Further, cell fate trajectory reconstruction and branch analysis using RNA Velocity or scFates can increase resolution from cell class to cell type, identifying type-related drivers, particularly for the highly heterogeneous amacrine, bipolar, and RGCs.

Using this atlas, we identified pro-survival factors, such as BDNF and GDNF, that can modify the retinal microenvironment to be more development-like, leading to modest recovery of vision (Figure 4E). However, once RGCs are lost, these factors alone cannot restore them. Stem cell technologies offer new avenues for cell replacement therapies. Clinical trials and research studies have shown the potential of retinal pigment epithelium and photoreceptor replacement to halt visual decline in age-related macular degeneration and cone/rod dystrophies *(41, 42)*. Similarly, glaucoma, a progressive neurodegenerative disease, could benefit from cell replacement to prevent or recover vision loss *(6)*. However, replacing the diverse class of RGCs is challenging due to the need for donor neurons to integrate into the host retina and extend axons toward the optic nerve head and brain.

Utilizing the atlas in stem-cell-derived products can aid in reference mapping and automated cell identity labeling. Since most organoids and 2D products remain at the progenitor or cell class-like genotype level, dataset annotation and product cell class identification are challenging. The atlas can serve as a reference tool for automated cell class/state identification, correlating in vitro time points with fetal development. By mapping cells from new datasets to the fetal atlas, we can identify differences and push the product toward the desired result, whether a specific timepoint, cell class/type/state, or cell yield.

RGC replacement by transplantation of primary or stem cell-derived RGCs is a potential approach to enable vision recovery within advanced-stage optic neuropathies *(6)*. Our previous work showed that more than 50% of healthy and even RGC-depleted recipient retinas retained donor RGCs post-transplant *(5)*. However, the number of surviving donor RGCs and retinal area covered by the transplant remained low. To address this challenge, we explore human retinal development using RGC transcriptomics to identify molecular features, including BDNF and GDNF, that may make the retinal microenvironment more pro-regenerative and support donor neuron survival. Consequently, we investigate using BDNF and GDNF as co-treatments to support the survival of donor cells within the diseased microenvironment.

A major limitation in delivering each factor is their rapid clearance and low bioavailability at the target site within the eye *(43, 44)*, necessitating frequent injections. To avoid these repeat injections, we formulated our donor RGCs with PODS for the sustained release of BDNF and GDNF. This approach increases not only the number of donor RGC but also the number of neurites extending into the optic nerve head (**Figures 4 and 5**). While

neurite outgrowth in xenotransplantation was less robust than in syngenetic transplantation, likely due to in vivo growth time differences, these findings suggest potential retina-to-brain rewiring, critical for functional recovery.

Modulating the host retinal microenvironment with sustained-release growth factors represents an innovative approach to improving transplantation outcomes. Furthermore, enhancing donor RGC morphology and axon outgrowth opens new possibilities in regenerative medicine for treating glaucoma and other optic neuropathies. Using neuroprotective factors in combination with other approaches to modify the retinal microenvironment and stem cell-derived RGC delivery may offer a viable solution to the challenge of RGC replacement. Depending on the model or state of the disease, the retinal microenvironment may also need to be altered to support donor RGC migration, growth, maturation, axon extension, and increased metabolic demands *(6, 17)*. Further exploration of our fetal retina atlas will lead to discovering and testing various cues to promote each of these key donor RGC functions. Integrating neuroprotective strategies with cell replacement therapies is a promising direction for research and clinical applications. Lastly, sustained-release growth factor formulations, such as PODS, represent a promising neuroprotective approach to limit RGC death before loss. Altogether, these findings provide promising insights into potential strategies for restoring vision lost due to RGC damage or loss in ONs.

Funding:

NIH/NEI–F32EY033211 (J.R.S.), NIH/NEI–L70EY034355 (J.R.S.), NIH/NEI–T32EY007145 (MBED fellowship, J.R.S.), NIH/NEI–5U24EY029893-03 (P.B.), NIH/NEI–P30EY003790 (Core Facility Grant), Bright Focus Foundation–G2020231 (P.B.), NIH/NEI R01EY021482 (T.A.R.), Gilbert Family Foundation–GFF00 (P.B.)

Author contributions:

J.R.S., E.K., J.O., M.P., J.M., C.P., and P.B. performed the research; J.R.S. and E.K. analyzed the data and created the figures; J.R.S. wrote the paper; and P.B. supervised the research.

Competing interests:

Christian Pernstich is an employee at Cell Guidance Systems, LTD.

References:

1. Y.-C. Tham, X. Li, T. Y. Wong, H. A. Quigley, T. Aung, C.-Y. Cheng, Global Prevalence of Glaucoma and Projections of Glaucoma Burden through 2040 A Systematic Review and Meta-Analysis. *Ophthalmology* **121**, 2081–2090 (2014).

2. L. Erskine, E. Herrera, Connecting the Retina to the Brain. *Asn Neuro* **6**, 1759091414562107 (2014).

3. K. Y. Zhang, E. A. Aguzzi, T. V. Johnson, Retinal Ganglion Cell Transplantation: Approaches for Overcoming Challenges to Functional Integration. *Cells* **10**, 1426 (2021).

4. P. Venugopalan, Y. Wang, T. Nguyen, A. Huang, K. J. Muller, J. L. Goldberg, Transplanted neurons integrate into adult retinas and respond to light. *Nat Commun* **7**, 10472 (2016).

5. J. Oswald, E. Kegeles, T. Minelli, P. Volchkov, P. Baranov, Transplantation of miPSC/mESC-derived retinal ganglion cells into healthy and glaucomatous retinas. *Mol Ther - Methods Clin Dev* **21**, 180–198 (2021).

6. J. R. Soucy, E. A. Aguzzi, J. Cho, M. J. Gilhooley, C. Keuthan, Z. Luo, A. Monavarfeshani, M. A. Saleem, X.-W. Wang, J. Wohlschlegel, T. Rr. Consortium, P. Baranov, A. D. Polo, B. Fortune, K. K. Gokoffski, J. L. Goldberg, W. Guido, A. L. Kolodkin, C. A. Mason, Y. Ou, T. A. Reh, A. G. Ross, B. C. Samuels, D. Welsbie, D. J. Zack, T. V. Johnson, Retinal ganglion cell repopulation for vision restoration in optic neuropathy: a roadmap from the RReSTORe Consortium. *Mol. Neurodegener.* **18**, 64 (2023).

7. L. Storgaard, T. L. Tran, J. C. Freiberg, A. S. Hauser, M. Kolko, Glaucoma Clinical Research: Trends in Treatment Strategies and Drug Development. *Frontiers Medicine* **8**, 733080 (2021).

8. S. Tehrani, L. Davis, W. O. Cepurna, T. E. Choe, D. C. Lozano, A. Monfared, L. Cooper, J. Cheng, E. C. Johnson, J. C. Morrison, Astrocyte Structural and Molecular Response to Elevated Intraocular Pressure Occurs Rapidly and Precedes Axonal

Tubulin Rearrangement within the Optic Nerve Head in a Rat Model. *Plos One* **11**, e0167364 (2016).

9. A. Sridhar, A. Hoshino, C. R. Finkbeiner, A. Chitsazan, L. Dai, A. K. Haugan, K. M. Eschenbacher, D. L. Jackson, C. Trapnell, O. Bermingham-McDonogh, I. Glass, T. A. Reh, Single-Cell Transcriptomic Comparison of Human Fetal Retina, hPSC-Derived Retinal Organoids, and Long-Term Retinal Cultures. *Cell Reports* **30**, 1644-1659.e4 (2020).

10. Y. Lu, F. Shiau, W. Yi, S. Lu, Q. Wu, J. D. Pearson, A. Kallman, S. Zhong, T. Hoang, Z. Zuo, F. Zhao, M. Zhang, N. Tsai, Y. Zhuo, S. He, J. Zhang, G. L. Stein-O'Brien, T. D. Sherman, X. Duan, E. J. Fertig, L. A. Goff, D. J. Zack, J. T. Handa, T. Xue, R. Bremner, S. Blackshaw, X. Wang, B. S. Clark, Single-Cell Analysis of Human Retina Identifies Evolutionarily Conserved and Species-Specific Mechanisms Controlling Development. *Dev. Cell* **53**, 473-491.e9 (2020).

11. S. Jin, C. F. Guerrero-Juarez, L. Zhang, I. Chang, R. Ramos, C.-H. Kuan, P. Myung, M. V. Plikus, Q. Nie, Inference and analysis of cell-cell communication using CellChat. *Nat Commun* **12**, 1088 (2021).

12. S. Jin, M. V. Plikus, Q. Nie, CellChat for systematic analysis of cell-cell communication from single-cell and spatially resolved transcriptomics. *bioRxiv* , 2023.11.05.565674 (2023).

13. L. Faure, R. Soldatov, P. V. Kharchenko, I. Adameyko, scFates: a scalable python package for advanced pseudotime and bifurcation analysis from single-cell data. *Bioinformatics* **39**, btac746 (2022).

14. H. Wickham, ggplot2, Elegant Graphics for Data Analysis. *R* (2016), doi:10.1007/978-3-319-24277-4.

15. N. Borcherding, A. Vishwakarma, A. P. Voigt, A. Bellizzi, J. Kaplan, K. Nepple, A. K. Salem, R. W. Jenkins, Y. Zakharia, W. Zhang, Mapping the immune environment in clear cell renal carcinoma by single-cell genomics. *Commun Biology* **4**, 122 (2021).

16. D. A. Barbie, P. Tamayo, J. S. Boehm, S. Y. Kim, S. E. Moody, I. F. Dunn, A. C. Schinzel, P. Sandy, E. Meylan, C. Scholl, S. Fröhling, E. M. Chan, M. L. Sos, K. Michel, C. Mermel, S. J. Silver, B. A. Weir, J. H. Reiling, Q. Sheng, P. B. Gupta, R. C. Wadlow, H. Le, S. Hoersch, B. S. Wittner, S. Ramaswamy, D. M. Livingston, D. M. Sabatini, M. Meyerson, R. K. Thomas, E. S. Lander, J. P. Mesirov, D. E. Root, D. G. Gilliland, T. Jacks, W. C. Hahn, Systematic RNA interference reveals that oncogenic KRAS-driven cancers require TBK1. *Nature* **462**, 108–112 (2009).

17. J. R. Soucy, L. Todd, E. Kriukov, M. Phay, V. V. Malechka, J. D. Rivera, T. A. Reh, P. Baranov, Controlling donor and newborn neuron migration and maturation in the eye through microenvironment engineering. *Proc. Natl. Acad. Sci.* **120**, e2302089120 (2023).

18. K. J. Wahlin, J. Cheng, S. L. Jurlina, M. K. Jones, N. R. Dash, A. Ogata, N. Kibria, S. Ray, K. C. Eldred, C. Kim, J. S. Heng, J. Phillips, R. J. Johnston, D. M. Gamm, C. Berlinicke, D. J. Zack, CRISPR Generated SIX6 and POU4F2 Reporters Allow Identification of Brain and Optic Transcriptional Differences in Human PSC-Derived Organoids. *Frontiers Cell Dev Biology* **9**, 764725 (2021).

19. C. M. Fligor, K.-C. Huang, S. S. Lavekar, K. B. VanderWall, J. S. Meyer, Differentiation of retinal organoids from human pluripotent stem cells. *Methods Cell Biol* **159**, 279–302 (2020).

20. R. Habibey, J. Striebel, F. Schmieder, J. Czarske, V. Busskamp, Long-term morphological and functional dynamics of human stem cell-derived neuronal networks on high-density micro-electrode arrays. *Front. Neurosci.* **16**, 951964 (2022).

21. A. P. Buccino, C. L. Hurwitz, S. Garcia, J. Magland, J. H. Siegle, R. Hurwitz, M. H. Hennig, SpikeInterface, a unified framework for spike sorting. *eLife* **9**, e61834 (2020).

22. P. Yger, G. L. Spampinato, E. Esposito, B. Lefebvre, S. Deny, C. Gardella, M. Stimberg, F. Jetter, G. Zeck, S. Picaud, J. Duebel, O. Marre, A spike sorting toolbox for up to thousands of electrodes validated with ground truth recordings in vitro and in vivo. *eLife* **7**, e34518 (2018).

23. S. Aibar, C. B. González-Blas, T. Moerman, V. A. Huynh-Thu, H. Imrichova, G. Hulselmans, F. Rambow, J.-C. Marine, P. Geurts, J. Aerts, J. van den Oord, Z. K. Atak, J. Wouters, S. Aerts, SCENIC: single-cell regulatory network inference and clustering. *Nat. Methods* **14**, 1083–1086 (2017).

24. K. T. Nguyen-Ba-Charvet, A. Rebsam, Neurogenesis and Specification of Retinal Ganglion Cells. *Int J Mol Sci* **21**, 451 (2020).

25. V. A. Traag, L. Waltman, N. J. van Eck, From Louvain to Leiden: guaranteeing well-connected communities. *Sci Rep-uk* **9**, 5233 (2019).

26. N. Shen, Y. Qu, Y. Yu, K.-F. So, A. M. Goffinet, N. Vardi, Y. Xu, L. Zhou, Frizzled3 Shapes the Development of Retinal Rod Bipolar Cells. *Investig. Opthalmology Vis. Sci.* **57**, 2788 (2016).

27. Y. Wang, D. Zhang, Y. Zhang, N. Ni, Z. Tang, Z. Bai, B. Shen, H. Sun, P. Gu, Insulin-like growth factor-1 regulation of retinal progenitor cell proliferation and differentiation. *Cell Cycle* **17**, 515–526 (2018).

28. A. Y. M. Wang, V. H. Y. Wong, P. Y. Lee, B. V. Bui, S. Dudczig, K. A. Vessey, E. L. Fletcher, Retinal ganglion cell dysfunction in mice following acute intraocular pressure is exacerbated by P2X7 receptor knockout. *Sci. Rep.* **11**, 4184 (2021).

29. B. J. Smith, X. Wang, B. C. Chauhan, P. D. Côté, F. Tremblay, Contribution of retinal ganglion cells to the mouse electroretinogram. *Doc Ophthalmol* **128**, 155–168 (2014).

30. D. Lowenstein, L. Arsenault, The effects of growth factors on the survival and differentiation of cultured dentate gyrus neurons. *J. Neurosci.* **16**, 1759–1769 (1996).

31. K. B. VanderWall, R. Vij, S. K. Ohlemacher, A. Sridhar, C. M. Fligor, E. M. Feder, M. C. Edler, A. J. Baucum, T. R. Cummins, J. S. Meyer, Astrocytes Regulate the Development and Maturation of Retinal Ganglion Cells Derived from Human Pluripotent Stem Cells. *Stem Cell Rep* **12**, 201–212 (2019).

32. M. Dinsdale, J. M. Guajardo-Beroiza, J. Mohamed-Noriega, N. A. Vallabh, Optic neuropathies that mimic glaucoma. *Community eye Heal.* **35**, 23–26 (2022).

33. A. Raharja, L. Whitefield, Clinical approach to vision loss: a review for general physicians. *Clin. Med.* **22**, 95–99 (2022).

34. W. W. Liu, M. A. Margeta, Imaging Retinal Ganglion Cell Death and Dysfunction in Glaucoma. *Int. Ophthalmol. Clin.* **59**, 41–54 (2019).

35. M. T. Pardue, R. S. Allen, Neuroprotective strategies for retinal disease. *Prog. Retin. Eye Res.* **65**, 50–76 (2018).

36. J. R. Tribble, F. Hui, H. Quintero, S. E. Hajji, K. Bell, A. D. Polo, P. A. Williams, Neuroprotection in glaucoma: Mechanisms beyond intraocular pressure lowering. *Mol. Asp. Med.* **92**, 101193 (2023).

37. M. Almasieh, L. A. Levin, Neuroprotection in Glaucoma: Animal Models and Clinical Trials. *Annu Rev Vis Sc* **3**, 1–30 (2016).

38. E. V. Mitroshina, T. A. Mishchenko, O. M. Shirokova, T. A. Astrakhanova, M. M. Loginova, E. A. Epifanova, A. A. Babaev, V. S. Tarabykin, M. V. Vedunova, Intracellular Neuroprotective Mechanisms in Neuron-Glial Networks Mediated by Glial Cell Line-Derived Neurotrophic Factor. *Oxidative Med. Cell. Longev.* **2019**, 1036907 (2019).

39. E. Palasz, A. Wysocka, A. Gasiorowska, M. Chalimoniuk, W. Niewiadomski, G. Niewiadomska, BDNF as a Promising Therapeutic Agent in Parkinson's Disease. *Int. J. Mol. Sci.* **21**, 1170 (2020).

40. A. C. Gauthier, J. Liu, Epigenetics and Signaling Pathways in Glaucoma. *BioMed Res. Int.* **2017**, 5712341 (2017).

41. S. R. Grob, A. Finn, T. D. Papakostas, D. Eliott, Clinical Trials in Retinal Dystrophies. *Middle East Afr. J. Ophthalmol.* **23**, 49–59 (2016).

42. V. Klymenko, O. G. G. Martínez, M. Zarbin, Recent Progress in Retinal Pigment Epithelium Cell-Based Therapy for Retinal Disease. *Stem Cells Transl. Med.* , szae004 (2024).

43. R. Varela-Fernández, V. Díaz-Tomé, A. Luaces-Rodríguez, A. Conde-Penedo, X. García-Otero, A. Luzardo-Álvarez, A. Fernández-Ferreiro, F. J. Otero-Espinar, Drug Delivery to the Posterior Segment of the Eye: Biopharmaceutic and Pharmacokinetic Considerations. *Pharmaceutics* **12**, 269 (2020).

44. A. Subrizi, E. M. del Amo, V. Korzhikov-Vlakh, T. Tennikova, M. Ruponen, A. Urtti, Design principles of ocular drug delivery systems: importance of drug payload, release rate, and material properties. *Drug Discov. Today* **24**, 1446–1457 (2019).

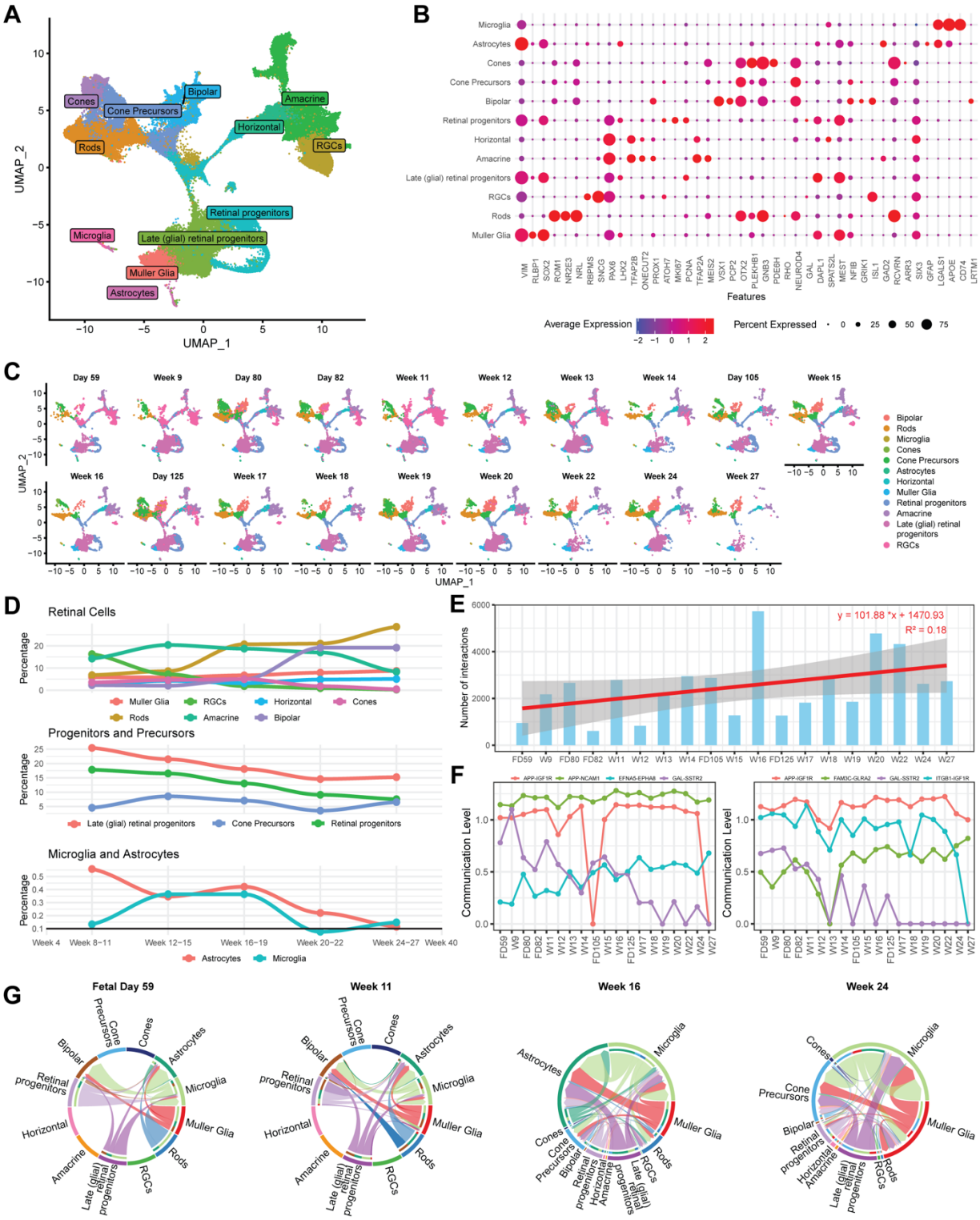

Figure 1. Cellular Composition and Communication in Human Fetal Retinal Development. (A) Integrated UMAP embedding demonstrating the cell types and their

distribution in the atlas of healthy human fetal retina from fetal week 8 to 27. **(B)** Dotplot representing the cell type-specific genes correlation with the annotated cell types in the dataset. **(C)** Dimplot split by time points shows differences in cell type enrichment during the development. **(D)** Cumulative cell type frequency plots demonstrate the timeline of cell types origin and dynamics in the retina for the major cell classes (top), progenitors and precursors (middle), and microglia and astrocytes (bottom). **(E)** Bar plot demonstrating the increasing number of interactions in the retinal development with regression line (in red) and standard error (in gray). The number of interactions represents the sum of every unique ligand-receptor interaction found to be present with the CellChat cell-cell interactions analysis. **(F)** Patterns of communication dynamics for representative ligand-receptor pairs from the total interactions obtained using an LRLoop analysis for the signaling from (left) and to (right) RGC across the development. **(G)** Chord diagrams for SPP1 ligand-receptor pairs across development, generated using CellChat analysis, show patterns of increasing signal complexity (from fetal day 59 to week 11) and new signaling cell types appearing (from week 11) during development. The diagrams visualize the interactions, where the outer circle stands for the cell class, the sector size demonstrates the contribution of the cell class to the signaling, and the inner circle shows the signaling receivers for every cell class. The arrows point in the signaling direction from sender to receiver, where the thickness of the arrow codes signaling strength.

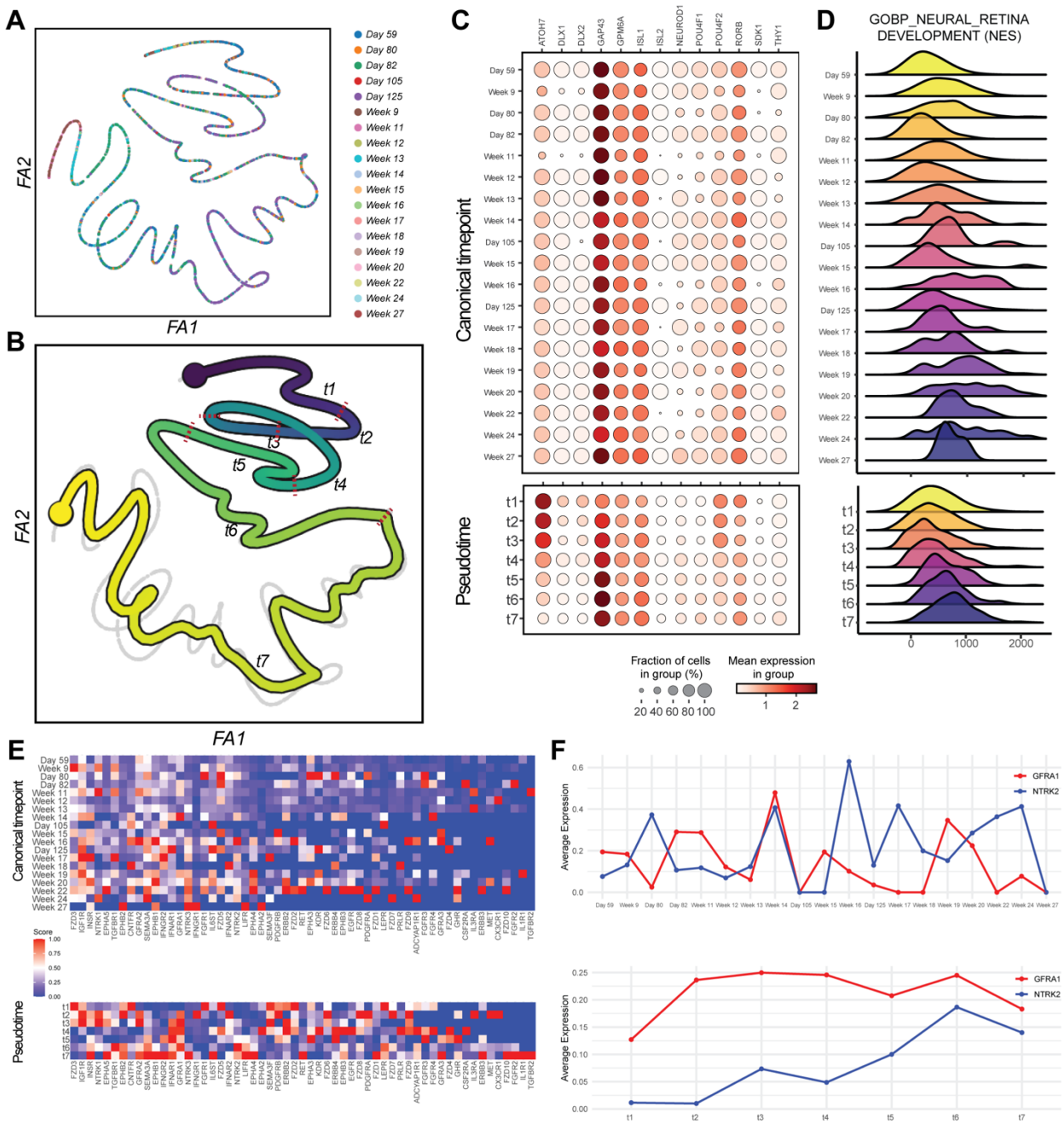

Figure 2. Temporal Gene Expression Dynamics of Retinal Ganglion Cell Differentiation During Human Fetal Development. (A) ForceAtlas2–based embedding of retinal ganglion cell from the fetal retina atlas. **(B)** Cell fate trajectory reconstructed with the scFates approach, with pseudotime values in color. For further analysis, pseudotime values were separated into seven sectors based on the automated predictive approach.

(C) Dotplot for the genes involved in the neural retina development shows the expression differences and gene gradients between the two approaches: the canonical time points separation on the top and pseudotime separation (that may include multiple canonical time points in every pseudotime sector) on the bottom. **(D)** Ridge enrichment plots for the neural retina development pathway upon GSEA analysis demonstrate the difference between the canonical timepoint- and pseudotime-based approaches. **(E)** Heatmap showing the expression patterns of neurotrophic receptors across the canonical time points and pseudotime sectors. Color codes the scaled and normalized expression values, with blue showing the lowest and red color – the highest values. **(F)** GFRA1 and NTRK2 neurotrophic receptor dynamics for the ordered canonical development timepoints and pseudotime sectors.

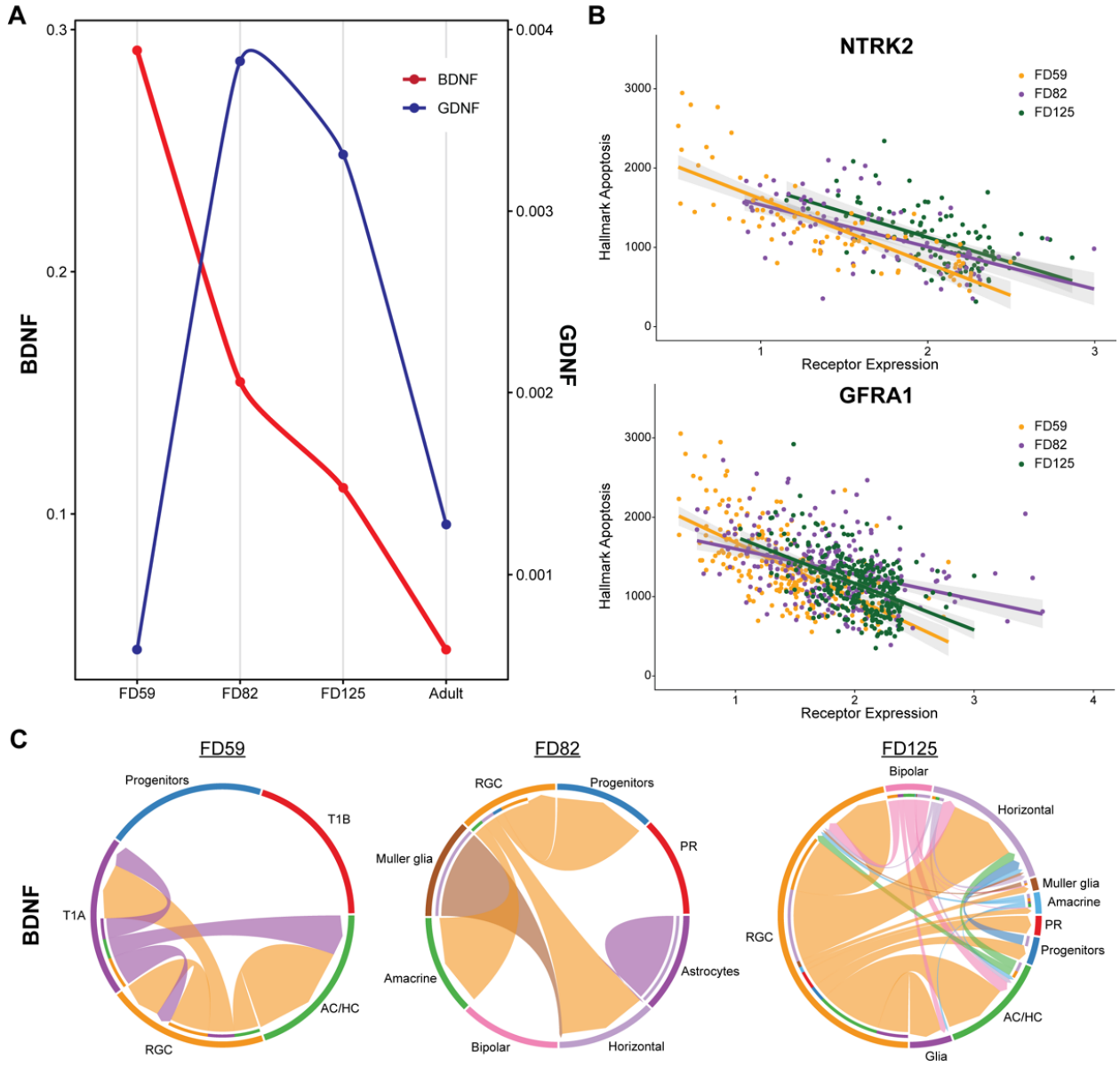

Figure 3. Characterization of neurotropic factors in retinal microenvironment during development. (A) BDNF and GDNF expression levels in the retina during different stages of development. **(B)** Correlation between BDNF and GDNF receptor expression and apoptotic genes. **(C)** Chord diagram showing cell-cell communication for the BDNF pathway.

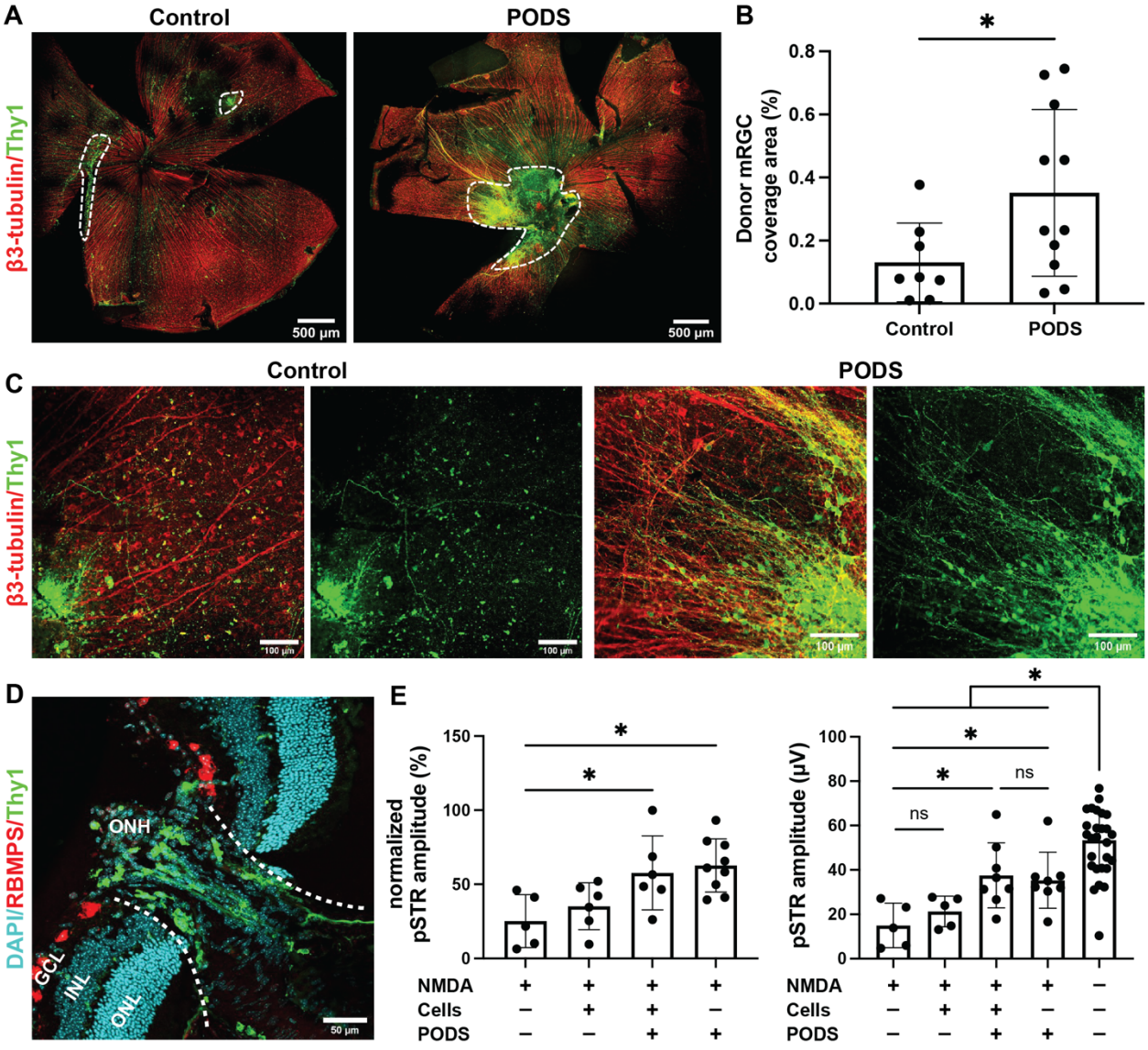

Figure 4. Mouse stem cell-derived RGC syngeneic transplantation in response to BDNF/GDNF co-treatment. (A) Representative retinal whole mount showing mouse donor RGC outgrowth (outlined) and **(B)** quantification of coverage area 2 weeks post-transplantation. **(C)** High magnification images showing mouse donor RGC neurite extensive outgrowth with BDNF/GDNF-PODS co-treatment. **(D)** Immunofluorescent image of a retinal section showing donor RGC entry into the optic nerve head (ONH) and down the optic nerve (outlines). GCL, ganglion cell layer; INL, inner nuclear layer; ONL,

1 outer nuclear layer. **(E)** Quantification of positive scotopic threshold response (pSTR)
2 measurements after transplantation and BDNF/GDNF-PODS co-treatment shows an
3 improvement in host RGC function in an NMDA-induced toxicity model as measured by
4 electroretinogram (ERG).

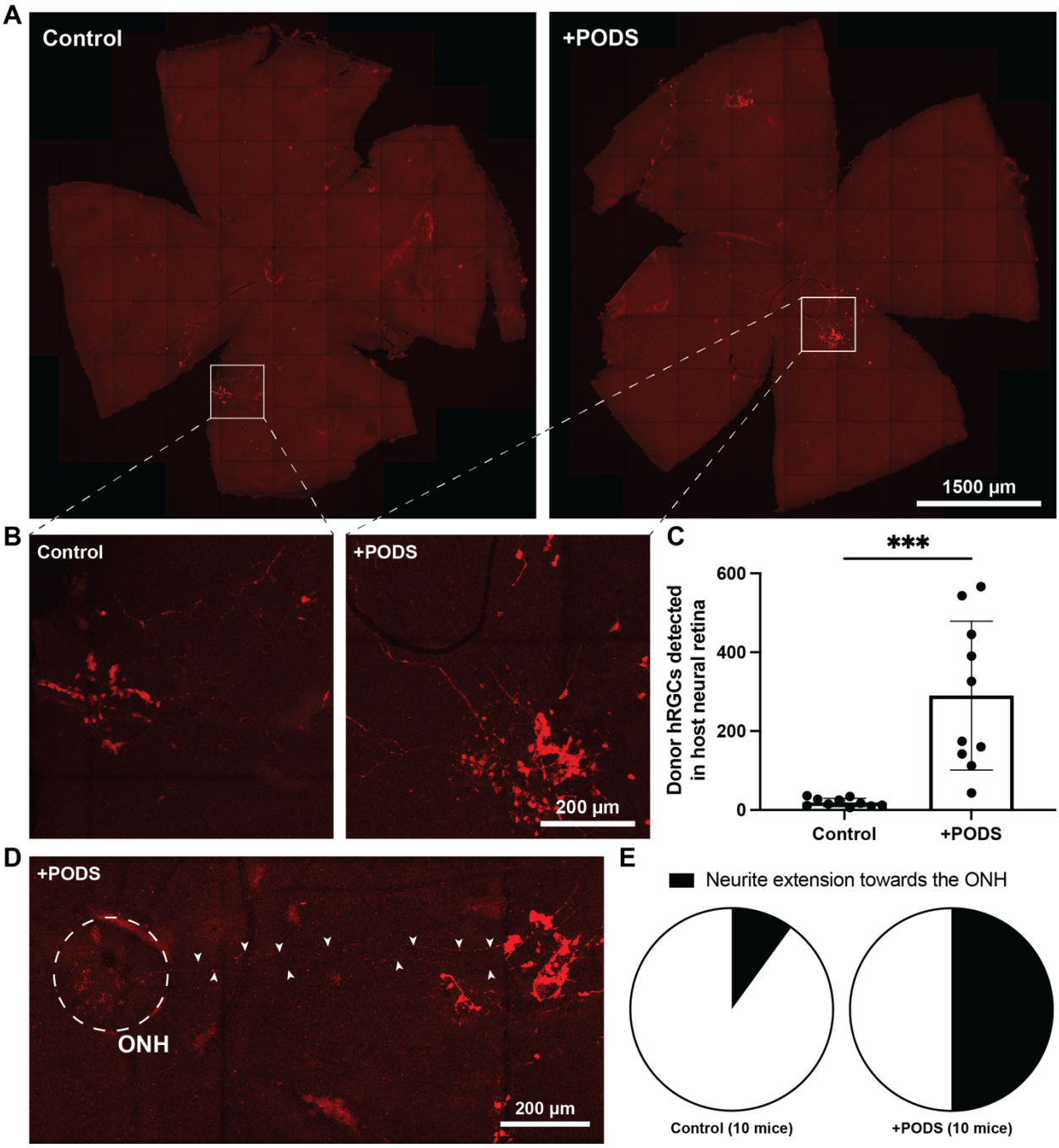

Figure 5. Human stem cell-derived RGC xenotransplantation in mice supplemented with sustained-release neurotrophic factors. (A) Representative retinal flat mounts and **(B)** high magnification images showing human donor RGC outgrowth (red). **(C)** Quantification of the number of donor RGCs detected in the host retina for RGCs

formulated with and without PODS. **(D)** Representative image of a retinal flat mount that highlights donor RGC neurite extension toward and into the optic nerve head (ONH). White arrows point to neurites extending the ONH. **(E)** Quantification of the number of transplanted retinas showing neurite extension toward the ONH with and without PODS co-treatment 3 days post-transplantation.

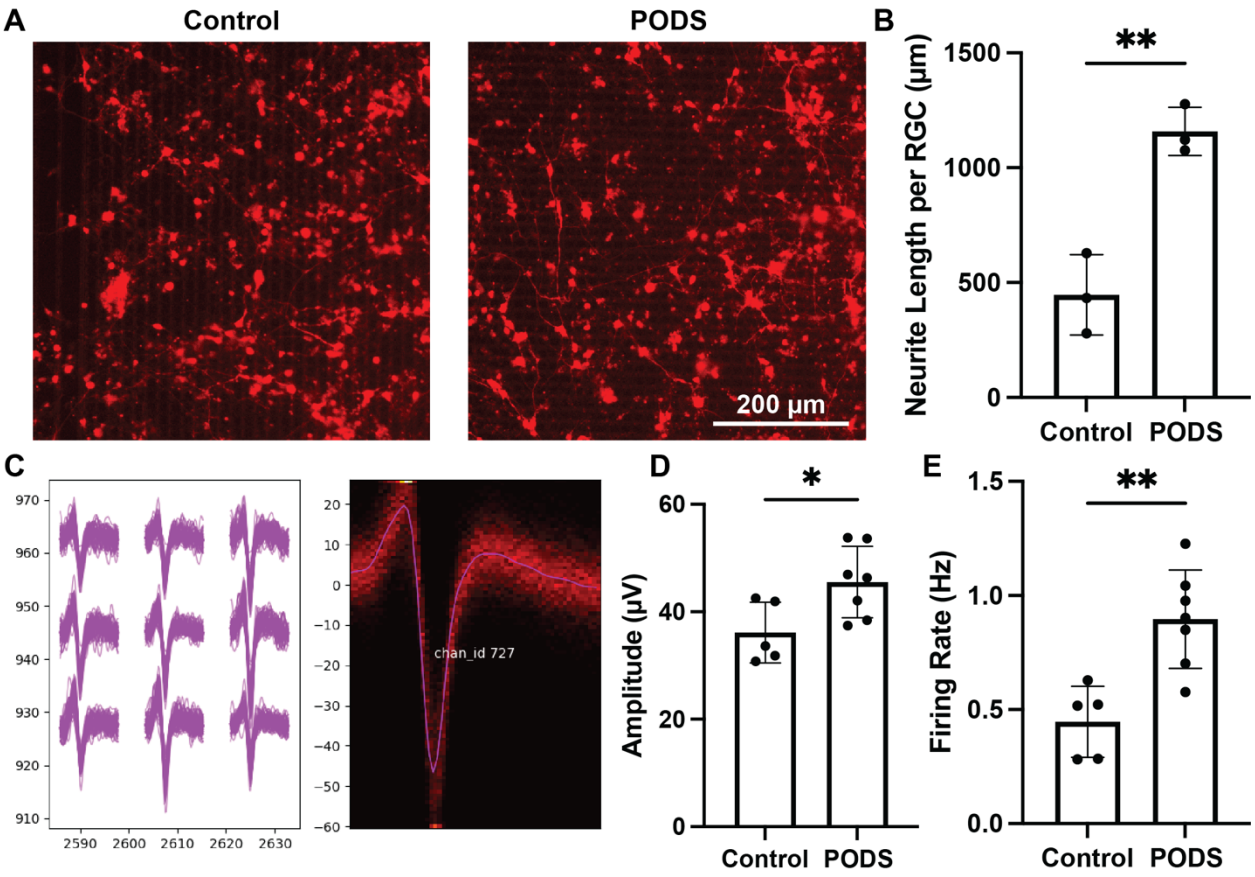

Figure 6. Human stem cell-derived RGC culture in response to BDNF/GDNF-PODS co-treatment. (A) Representative fluorescent images of td-Tomato positive RGCs cultured on an MEA with and without BDNF/GDNF-PODS. **(B)** Quantification of neurite outgrowth after 1 week in culture. **(C)** Representative spontaneous RGC action potentials recorded from multiple electrodes corresponding to a single neuron. **(D)** Quantification of median amplitude and **(E)** mean spontaneous firing rate measured from all the individual neurons cultured in an MEA with and without BDNF/GDNF-PODS.

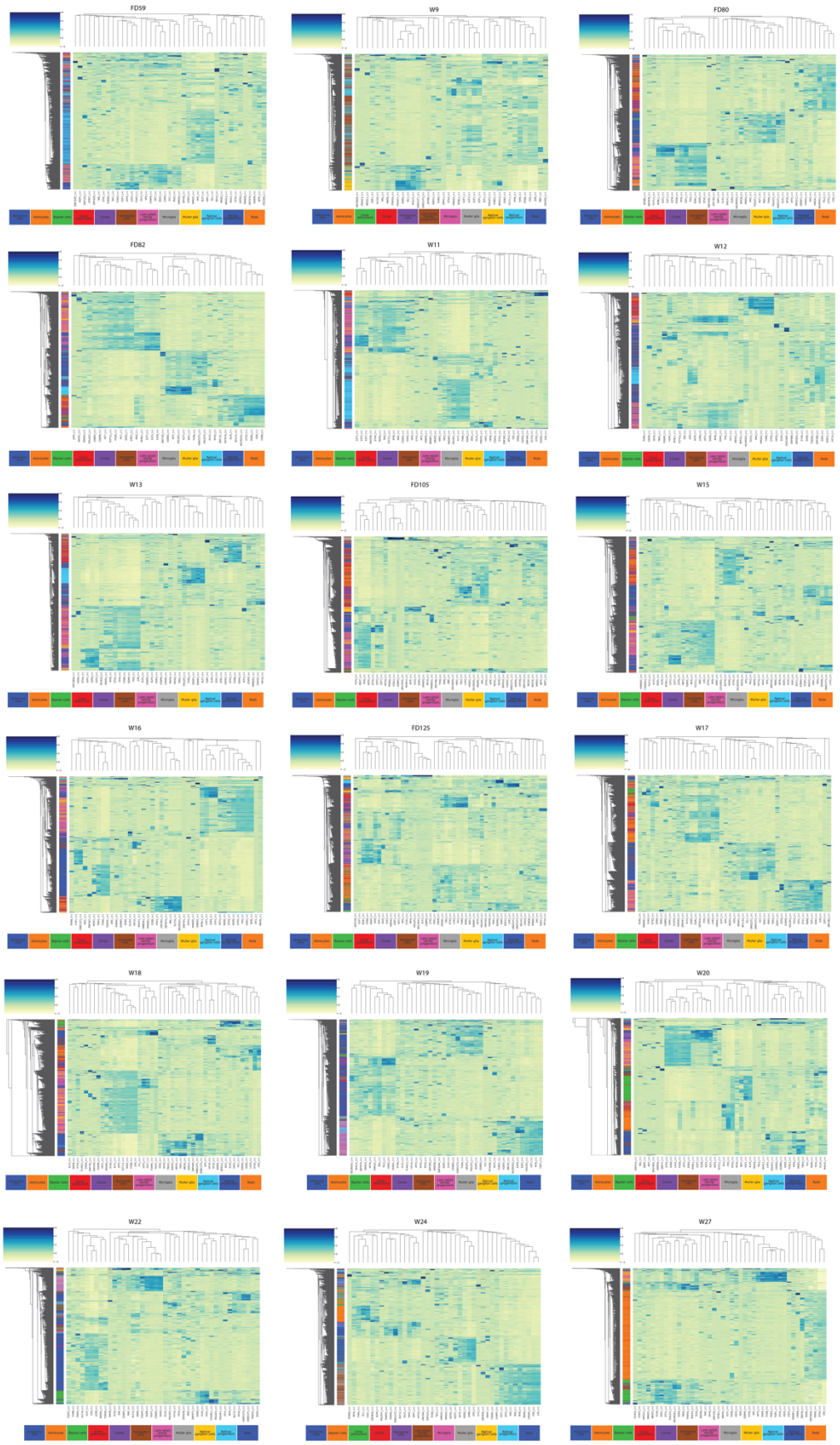
FD59
W9
FD80
FD82
W11
W12
W13
FD105
W15
W16
FD125
W17
W18
W19
W20
W22
W24
W27

1

1 **Figure S1. Timepoint/cell class resolution panels representing expression of**

2 **variable regulons within the atlas.**

3

Figure S2. Top-5 regulons for every timepoint and cell class upon pySCENIC analysis demonstrate both conservative and variable regulons in developmental dynamics.

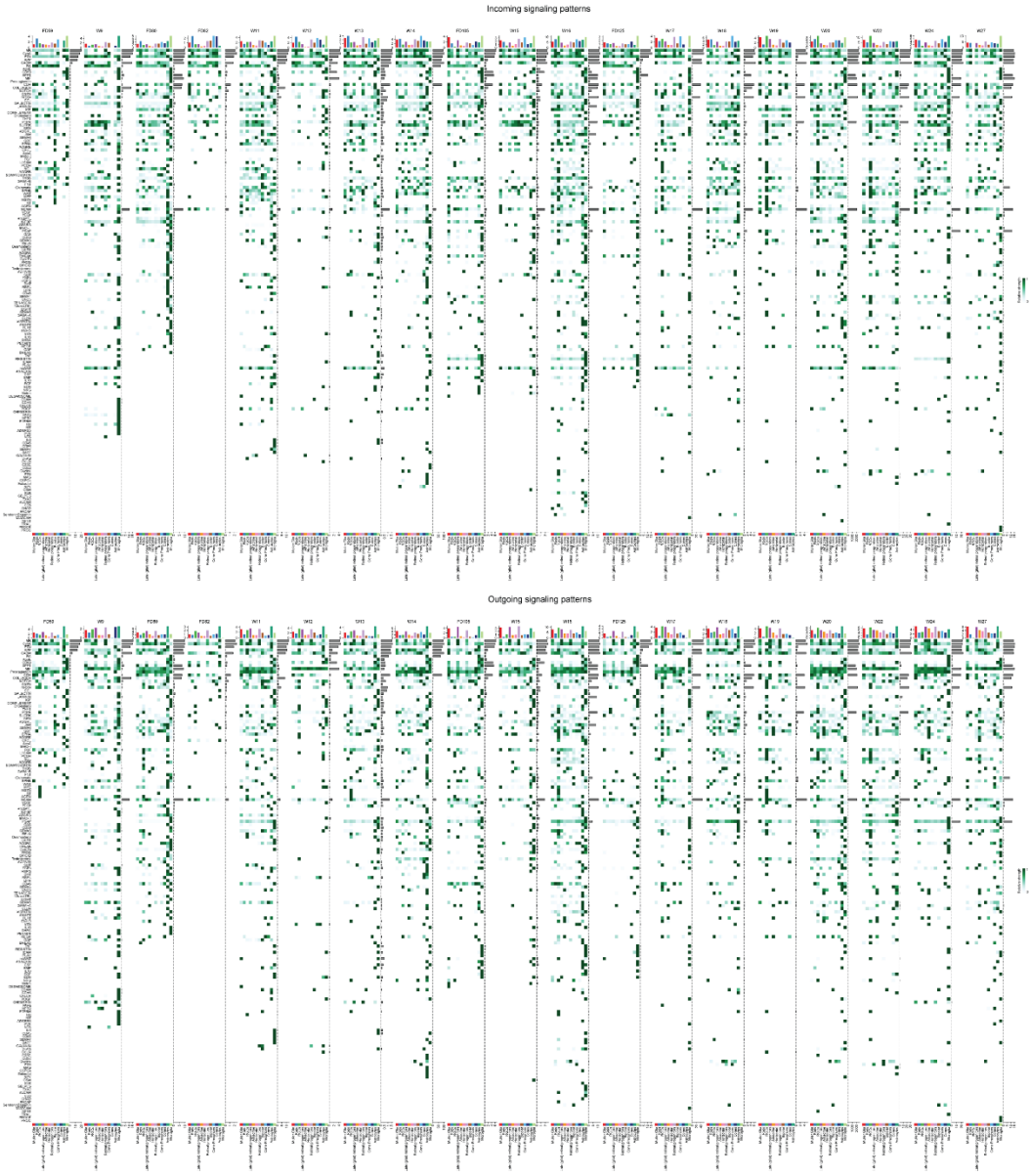

Figure S3. Cell-cell interactions in retinal development. Complete panel demonstrating all the incoming and outgoing cell-cell interactions for every cell class and every timepoint in the generated human fetal retinal atlas using the CellChat analysis.

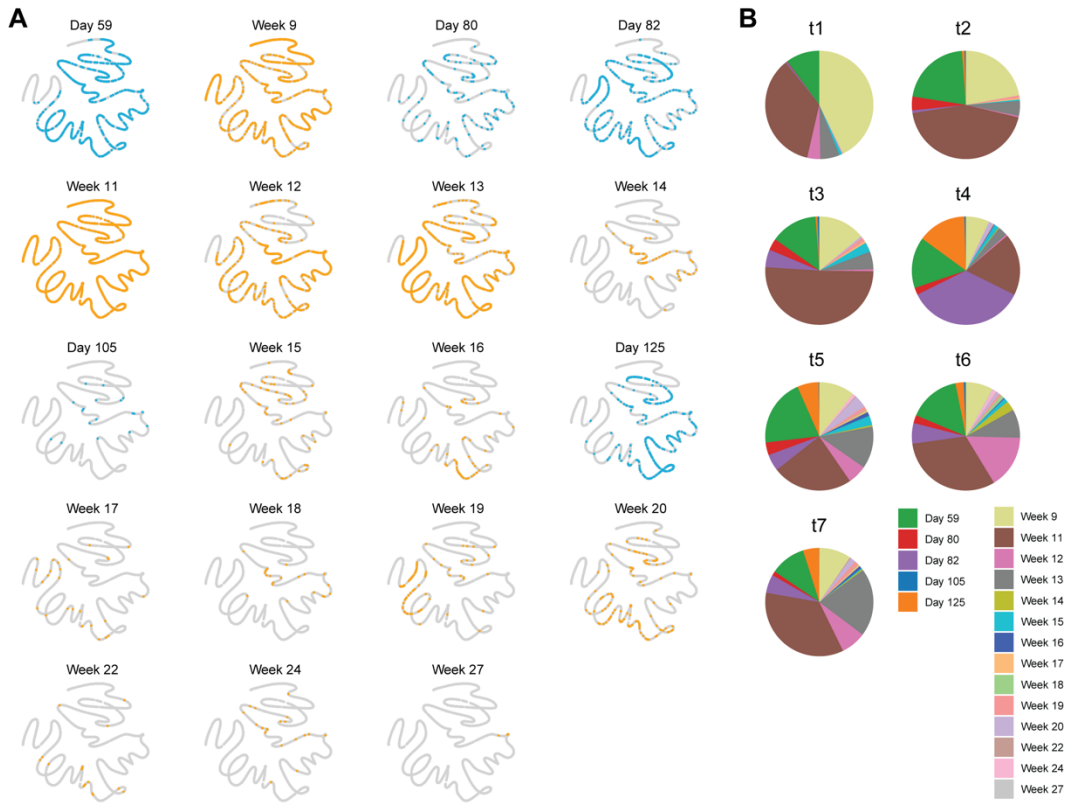

Figure S4. Sourcing of RGCs for ForceAtlas2-based embeddings. (A) Distribution of retinal ganglion cells across the time points on the UMAP embedding. Color codes the public source of the data. **(B)** Pie charts showing the distribution of the time points for every pseudotime sector.

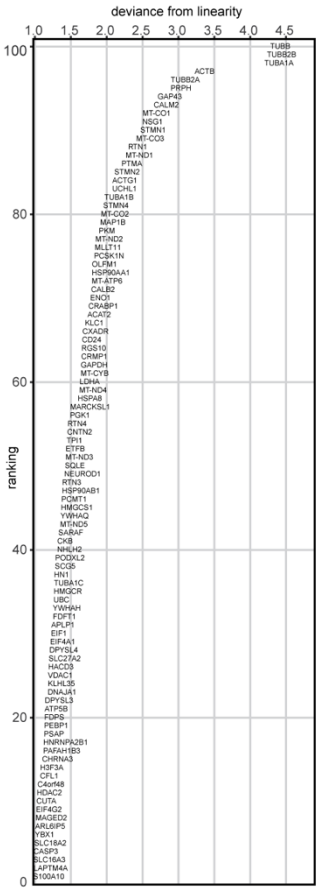

Figure S5. RGC variable gene expression pattern along the cell fate trajectory. The deviance from the linearity parameter codes the distance from the root to the end of the trajectory.

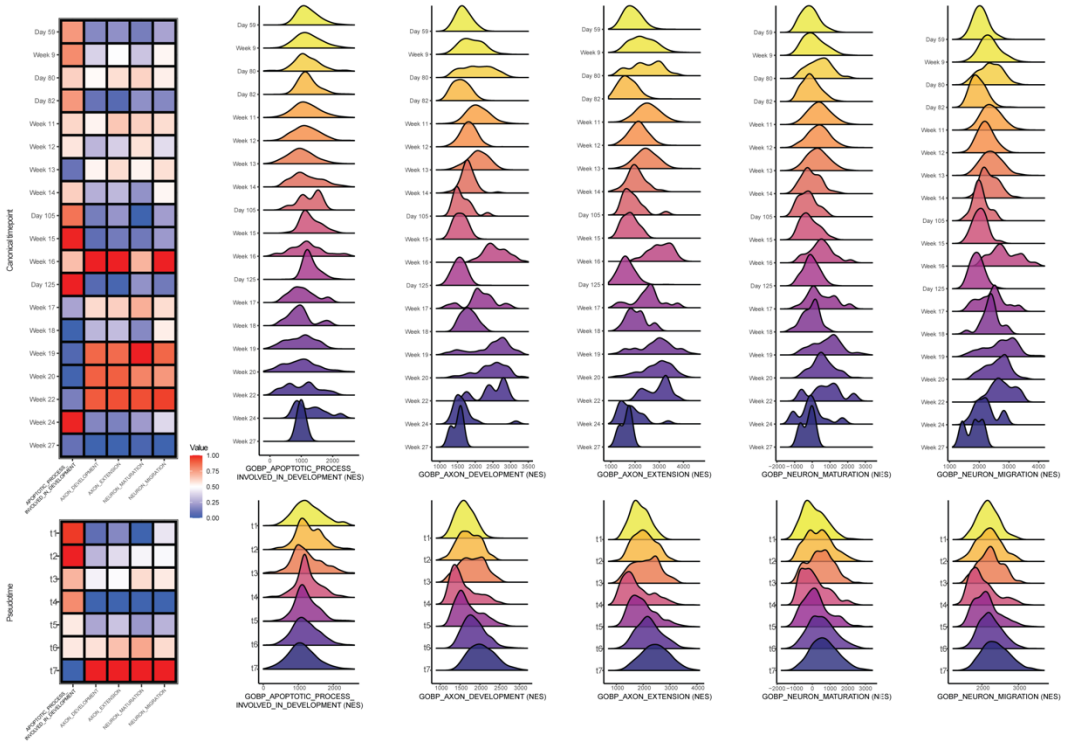

Figure S6. Tissue- and Cell-level RGC pathway analysis during development. Cumulative double-normalized GSEA pathway analysis enrichment scores representing the timeframes for the pathway activity between canonical timepoint- and pseudotime-based approaches. Separated ridge enrichment plots comparing the pathway activity between canonical timepoint- and pseudotime-based approaches for GOBP_APOPTOTIC_PROCESS_INVOLVED_IN_DEVELOPMENT, GOBP_AXON_ DEVELOPMENT, GOBP_AXON_EXTENSION, GOBP_NEURON_ MATURATION, GOBP_NEURON_MIGRATION.

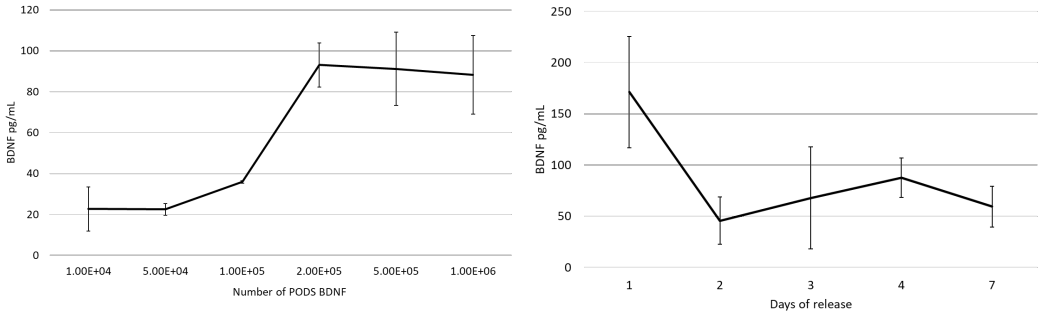

Figure S7. Release Kinetics of BDNF from PODS crystals. The availability of BDNF in the cell culture medium, released from PODS® Human BDNF, is both time- and dose-dependent.

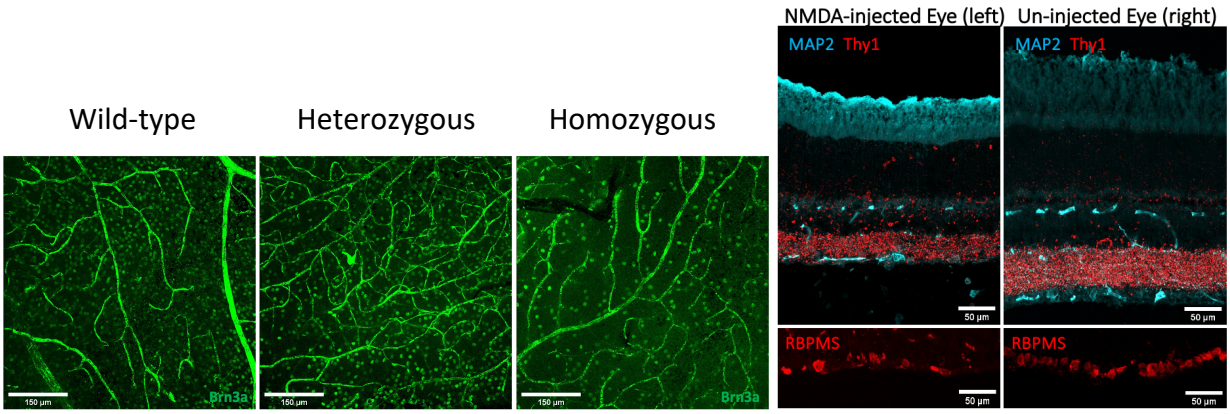

Figure S8. Inherited loss or neurotoxic mouse models. Representative fluorescent images of retinal flat mounts and sections showing RGC loss in an inherited loss model (homozygous) and neurotoxic models (NMDA-injected).

1

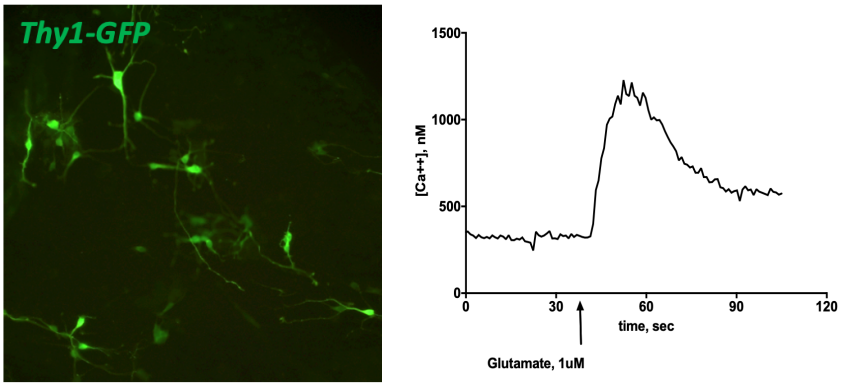

2 **Figure S9. Mouse stem cell-derived RGC function.** Mouse stem cell-derived RGC

3 function was evaluated using Ca2+ imaging (Fura-2 AM) in response to 1uM Gluatmate.

4

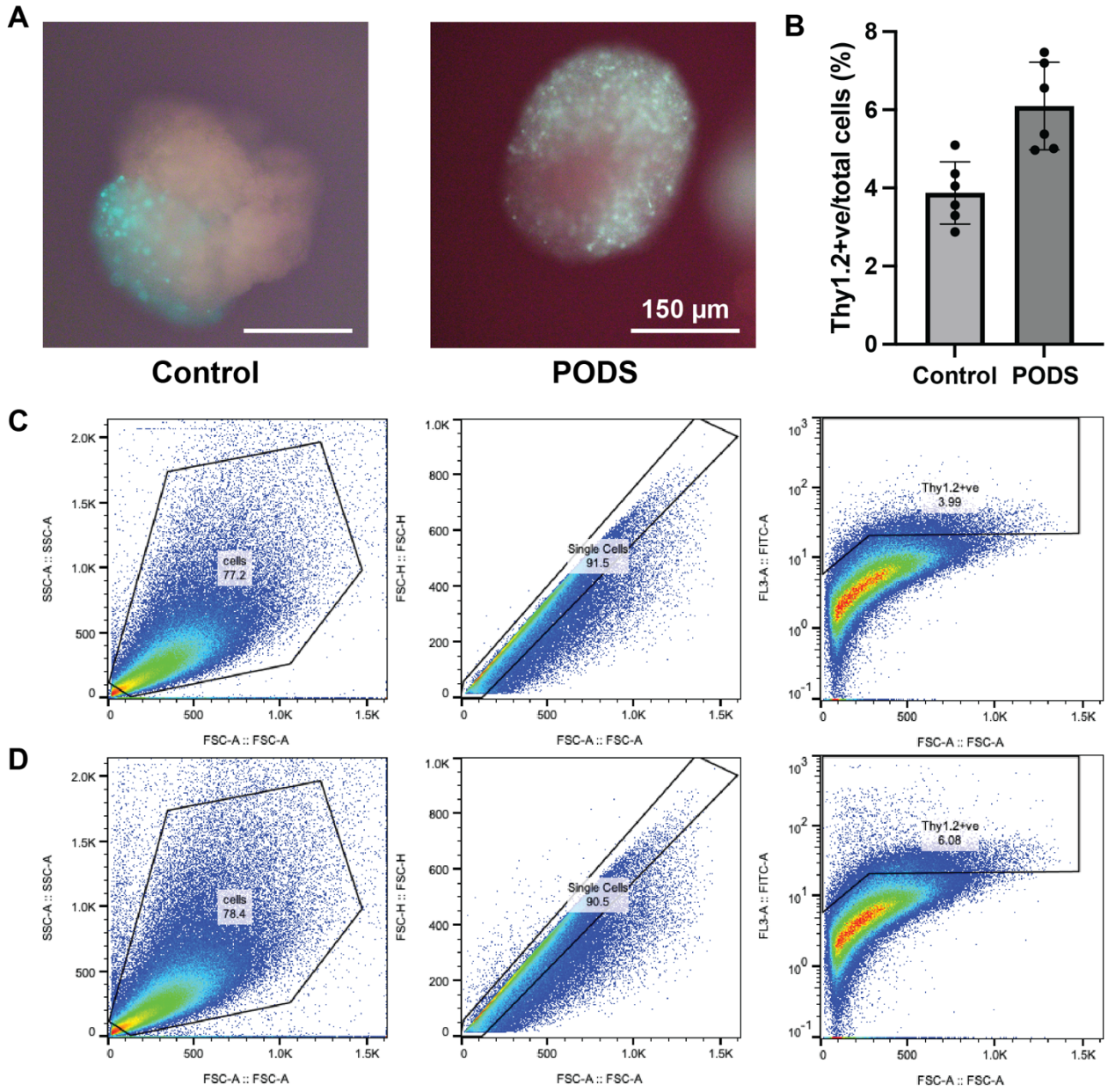

Figure S10. Slow-release BNDF and GDNF improve RGC differentiation yield. (A) Representative fluorescent image of late-stage (D27) mouse retinal organoids with and without PODS co-treatment during the differentiation. **(B)** Thy1.2+ve yield is increased in response to PODS co-treatment as measured by flow cytometry compared to controls. **(C)** Representative FACS plots with gating for dissociated mouse retinal organoids in the control group vs. **(D)** the PODS group.

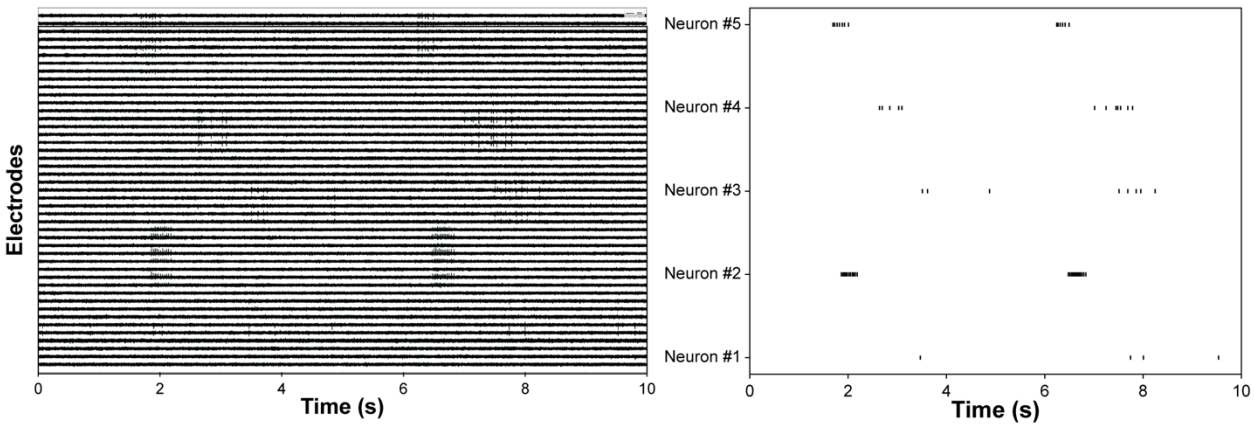

Figure S11. Spike sorting human RGC action potentials using a high-density multielectrode array. Representative traces from preprocessing MEA recordings of spontaneous RGC action potentials from individual electrodes after 18 – 20 days in culture and accompanying raster plot showing five neurons identified after spike sorting the raw traces.

1 **Table S1. Software packages for single-cell RNA sequencing analysis**

Software /package	Version	Link
R	4.2.1-4.3.1	https://cran.r-project.org/bin/
RStudio	2022.07.2-2023.06.1	https://www.rstudio.com/products/rstudio/download/
Azimuth	0.4.6	https://github.com/satijalab/azimuth
biomaRt	2.52.0-2.56.1	https://bioconductor.org/packages/release/bioc/html/biomaRt.html
CellChat	1.5.0-2.1.0	https://github.com/sqjin/CellChat
ComplexHeatmap	2.16.0	https://bioconductor.org/packages/release/bioc/html/ComplexHeatmap.html
cowplot	1.1.1	https://cran.r-project.org/web/packages/cowplot/
dittoSeq	1.8.1-1.12.2	https://bioconductor.org/packages/release/bioc/html/dittoSeq.html

dplyr	1.0.10-1.1.3	https://dplyr.tidyverse.org/
escape	1.5.1-1.6.0	https://github.com/ncborcherding/escape
future	1.33.0	https://cran.r-project.org/web/packages/future/index.html
ggalt	0.4.0	https://yonicd.github.io/ggalt/index.html
ggplot2	3.3.6-3.4.3	https://ggplot2.tidyverse.org/
GSEABase	1.58.0-1.62.0	https://bioconductor.org/packages/release/bioc/html/GSEABase.html
htmlwidgets	1.5.4-1.6.2	https://www.htmlwidgets.org/
LRLoop	0.1.0	https://github.com/Pinlyu3/LRLoop
Matrix	1.5-1-1.6-0	https://cran.r-project.org/web/packages/Matrix/index.html
patchwork	1.1.2-1.1.3	https://patchwork.data-imaginist.com/
plotly	4.10.0	https://plotly.com/r/
reticulate	1.26-1.32.0	https://rstudio.github.io/reticulate/

SCopeLoomR	0.13.0	https://github.com/aertslab/SCopeLoomR
sctransform	0.4.0	https://github.com/satijalab/sctransform
Seurat	4.2.0-4.3.1	https://satijalab.org/seurat/
SeuratDisk	0.0.0.9020	https://github.com/mojaveazure/seurat-disk
Python	3.7.4	https://www.python.org/
anndata	0.8.0	https://anndata.readthedocs.io/
loompy	3.0.7	https://linnarssonlab.org/loompy/
matplotlib	3.5.3	https://matplotlib.org/
numpy	1.21.6	https://numpy.org/
palantir	1.2	https://pypi.org/project/palantir/
pandas	1.3.5	https://pandas.pydata.org/
pySCENIC	0.12.1	https://pyscenic.readthedocs.io/
scanpy	1.9.3	https://scanpy.readthedocs.io/
scFates	1.0.6	https://scfates.readthedocs.io/en/latest/
seaborn	0.12.2	https://seaborn.pydata.org/

1 **Table S2. Primary antibodies for immunohistochemistry**

Antibody	Concentration	Vendor	Catalog #
Chicken Anti-mCherry	1:500	Abcam	ab205402
Chicken Anti-GFP	1:50	enQuire BioReagents	NC1666473
Rabbit Anti-RBPMS	1:300	GeneTex	GTX118619
Mouse Anti-Thy1	1:400	Serotec	MCA02R
Rabbit Anti-Map2	1:250	Biolegend	840601
Anti-Osteopontin	1:250	Hybridoma Bank	MPIIIB10(1)
Rabbit Anti-Melanopsin	1:400	Santa Cruz	sc-32870
Mouse B3-tubulin	1:500	Sigma Aldrich	T8660
Mouse Brn3a	1:500	Millipore	MAB1585

2